

MEASUREMENT OF HYDRODYNAMIC BOUNDARY CONDITIONS AND
VISCOSITY OF LIPID MEMBRANES

by

PHILIP ELIAS JAHL

A DISSERTATION

Presented to the Department of Physics
and the Division of Graduate Studies of the University of Oregon
in partial fulfillment of the requirements
for the degree of
Doctor of Philosophy

June 2021

DISSERTATION APPROVAL PAGE

Student: Philip Elias Jahl

Title: Measurement of Hydrodynamic Boundary Conditions and Viscosity of Lipid Membranes

This dissertation has been accepted and approved in partial fulfillment of the requirements for the Doctor of Philosophy degree in the Department of Physics by:

Benjamin McMorran	Chairperson
Raghuveer Parthasarathy	Advisor
Jayson Paulose	Core Member
Scott Hansen	Institutional Representative

and

Andy Karduna	Interim Vice Provost for Graduate Studies
--------------	---

Original approval signatures are on file with the University of Oregon Division of Graduate Studies.

Degree awarded June 2021

© 2021 Philip Elias Jahl
This work is licensed under a Creative Commons
Attribution-NonCommercial-NoDerivs (United States) License.



DISSERTATION ABSTRACT

Philip Elias Jahl

Doctor of Philosophy

Department of Physics

June 2021

Title: Measurement of Hydrodynamic Boundary Conditions and Viscosity of Lipid Membranes

Cell membranes have a difficult role - they must be able to separate and protect the interior of the cell from its environment, but they also must be able to selectively allow desired materials in and waste out, while remaining flexible and being able to grow. This range of functions is accomplished with a complicated and dynamic mixture of lipids and proteins. While the proteins are responsible for specific tasks, it is the lipids that determine the structure of the membrane and their fluidity that allows the embedded proteins to arrange themselves. Understanding lipid fluid properties is therefore important in order to have a full picture of cellular dynamics.

We examine the interaction between a lipid bilayer and the surrounding fluid in order to measure the boundary conditions. With an extremely precise measurement of the diffusion of giant unilamellar vesicles we are able to use the

Stokes-Einstein relation to determine that despite its fluidity, a lipid membrane has boundary conditions that match those of a solid.

Next we assess the accuracy of a technique used to measure the viscosity of a membrane using elliptical beads by performing it simultaneously with an established technique using the motion of phase separated domains. After showing its reliability we apply it to determine if there is any viscosity dependence on lipid chain length, which would be impossible using the phase separated domain method. We find that there is a small increase in viscosity with chain length.

We also examine the effect a recently discovered protein, β cell expansion factor A, or BefA, has on membrane morphology. We find that it causes membrane budding, resulting in clusters of small vesicles adhered to the outside of a larger one.

This dissertation contains previously published and unpublished material.

CURRICULUM VITAE

NAME OF AUTHOR: Philip Elias Jahl

GRADUATE AND UNDERGRADUATE SCHOOLS ATTENDED:

University of Oregon, Eugene, Oregon
Harvey Mudd College, Claremont, California

DEGREES AWARDED:

Doctor of Philosophy, Physics, 2021, University of Oregon
Bachelor of Science, Physics, 2016, Harvey Mudd College

AREAS OF SPECIAL INTEREST:

Membrane Physics
Image Analysis

PROFESSIONAL EXPERIENCE:

Graduate Research Assistant, Parthasarathy Lab, University of Oregon,
Eugene, Oregon, 2017-2021

Graduate Teaching Fellow, Department of Physics, University of Oregon,
Eugene, Oregon, 2016-2017

PUBLICATIONS:

Hill, J. H. & Massaquoi, M. S. & Sweeney, E. G. & Wall, E. & Jahl, P. E.
& Kallio, K. & Derrick, D. & Bell, R. & Murtaugh, L. C. & Parthasarathy,
R. & Remington, S. J. & Round, J. L. & Guillemain, K. (2021). Host and
microbe derived membrane permeabilization proteins increase β -cell mass
(under review)

Jahl, P. E & Parthasarathy, R. (2020). Lipid Bilayer Hydrodynamic Drag
Physical Review Research 2, 013132.

ACKNOWLEDGEMENTS

None of the research in this dissertation would have been possible without the support and guidance of my advisor, Dr. Raghuv eer Parthasarathy. His mentorship has shaped not just my work, but the type of scientist I want to be. I would also like to thank the members of the lab who made the work fun and collaborative, including Christopher Dudley, Ryan Baker, Savannah Logan, Brandon Schlomann, Teddy Hay, Deepika Sundarraman, Julia Ngo, Jonah Sokoloff, Vivek Ramakrishna, Noah Pettinari, Dylan Martins, and Vince Thoms. Thank you to my thesis committee for their support. Thanks also to Dr. Emily Goers Sweeney for her partnership in my work involving BefA.

Many thanks are also owed to my friends, my family, and my partner. In a very real way this work would not have been possible without their tireless support and encouragement.

For my parents, who taught me to love the natural world and to examine it.

TABLE OF CONTENTS

Chapter	Page
I. LIPIDS, MEMBRANES, AND VESICLES	1
1.1. Introduction	1
1.2. Lipids	2
1.3. Membranes	4
1.4. Vesicles	8
1.5. Conclusion	11
II. LIPID BILAYER HYDRODYNAMIC DRAG	12
2.1. Introduction	12
2.2. Methods	15
2.3. Results	20
III. COMPARISON OF MICRORHEOLOGICAL METHODS FOR MEASURING LIPID MEMBRANE VISCOSITY	24
3.1. Introduction	24
3.2. Experimental Methods	27
3.3. Image Analysis	29
3.4. Mathematical Analysis	30
3.5. Results	34

Chapter	Page
3.6. Chain Length	37
3.7. Conclusion	40
IV. MEMBRANE INTERACTIONS OF THE β CELL EXPANSION FACTOR A PROTEIN	43
4.1. Microbiota and Model Organisms	43
4.2. β Cells and Bacteria	44
4.3. BefA and Membrane Morphology	45
4.4. Continuing Work	46
V. CONCLUSIONS AND FUTURE DIRECTIONS	49
REFERENCES CITED	51

LIST OF FIGURES

Figure	Page
1.1. Bond line models of four example lipids, showing differences in head group, saturation, and chain length. Images taken from Avanti Lipids.	4
1.2. A schematic of the phases of lipid membranes – from the top, pseudocrystalline (L_C), gel (L_β), ripple (P_β), liquid disordered (L_D) . . .	6
1.3. A schematic of the liquid ordered phase achieved by adding cholesterol when above the melting temperature (top) or below the melting temperature (bottom)	7
1.4. Top: A schematic of a supported lipid bilayer and Bottom: a black lipid membrane	9
1.5. A schematic of vesicle creation using electroformation. Lipids deposited on ITO coated glass slides and a sucrose solution is placed between them. The slides are connected to an alternating voltage source, creating an oscillating electric field that encourages vesicle formation.	11
2.1. (a) A schematic of the setup for light sheet fluorescence microscopy of vesicle diffusion. The excitation laser is shown entering the sample chamber from the left as it is focused into a thin sheet. Light emitted by the sample is collected by the objective lens shown behind the cuvette. (b) A typical light sheet fluorescence image of the central plane of a 15 μm diameter polystyrene microsphere. (c) Histogram of C for 29 particles, giving a mean \pm standard error of $C = 6.28 \pm 0.15$. (d) A typical light sheet fluorescence image of the central plane of a fluorescein-dyed water droplet in benzyl alcohol. (e) Histogram of C values for 25 droplets, giving a mean \pm standard error of $C = 4.36 \pm 0.29$. In (b) and (d), the dashed-dotted line indicates the theoretical value of $C = 4.27$ for water in benzyl alcohol and the dashed and dotted lines respectively indicate the theoretical values of $C = 6$ and $C = 4$ for the boundary conditions of a rigid sphere and an inviscid (zero shear stress) sphere.	22
2.2. (a) A typical light sheet fluorescence image of the central plane of a DOPC vesicle. (b) Mean-square-displacements from 10 randomly	

Figure	Page
<p>chosen vesicle trajectories (colored lines), along with their average (dashed gray line). (c) Histogram of the reduced χ^2 values for each vesicle; $\chi^2 = 1$ indicates purely diffusive motion. (d) Histogram of C for 26 vesicles giving a mean \pm standard error of $C = 5.92 \pm 0.13$. The dashed and dotted lines indicate the theoretical values of $C = 6$ and $C = 4$ for the boundary conditions of a rigid sphere and an inviscid (zero shear stress) sphere.</p>	23
<p>3.1. A schematic of beads bound to a membrane. It is not obvious if the effective radius is small, as on the left where there is a small binding site, or large, as on the right where there is a large induced curvature.</p>	24
<p>3.2. An example image of the pole of a vesicle that has undergone phase separation with bright liquid-disordered domains in the main liquid-ordered phase. Imaged at room temperature, and comprised of DPPC, DOPC,Cholesterol, DOTAP, 16:0 Biotinyl PE, and Texas Red DHPE</p>	26
<p>3.3. On the left, a pair of beads form a non-spherical tracer. A membrane containing biotin binds to a neutravidin coated bead, which in turn is bound to a biotin coated bead. On the right, a single elliptical bead coated with neutravidin binds to the membrane, but does not form a circular inclusion.</p>	27
<p>3.4. A schematic of the device used for stretching beads, before and after stretching, with the actual device.</p>	29
<p>3.5. Translational diffusion coefficient vs. the rotational diffusion coefficient with curves of constant viscosity based on the HPW model. Many of the points fall outside the allowed region because the inclusions are not rotationally symmetric.</p>	33
<p>3.6. Parallel diffusion coefficient vs. the rotational diffusion coefficient with curves of constant viscosity based on the LLM model.</p>	34
<p>3.7. A histogram of the effective bead lengths L with the nominal length shown with a dotted vertical line. There is one bead with $L = 6.4 \mu\text{m}$ which is not shown in order to provide more detail.</p>	36
<p>3.8. All viscosity values for the domains and beads with the mean \pm standard error plotted.</p>	37

Figure	Page
3.9. A plot taken from [1] showing diffusion coefficients of lipid analogue DiD and proteins LacY and GltT	38
3.10. A histogram of the effective bead lengths from all chain lengths combined.	40
3.11. All viscosity values for the each chain length with the mean \pm standard error plotted. Fitting a line to the data has the slope $1.9 \pm 1.8 \times 10^{-10}$ implying a very weak, but positive affect on viscosity.	41
3.12. Comparison of the viscosity at each chain length as measured with elliptical beads (grey x's) and viscosity calculated using lipid diffusion values from [1] and the Saffmann-Delbrück model (red squares). All viscosities are normalized to the 14 chain length value. Despite an order of magnitude difference in viscosity the trend is very similar. . . .	42
4.1. An example control vesicle and multi-vesicular vesicle. Both scale bars are $10 \mu\text{m}$. This figure is taken from an unpublished co-authored work.	47
4.2. (a) The percentage of observed features that were multi-vesicular in the control and $2 \mu\text{M}$ BefA. Each point is a single scan. The bars represent the total percentage across all scans, 3% in the control and 30% in BefA treated. (b) The concentration of features in each scan, showing an increase with BefA exposure. This figure is taken from an unpublished co-authored work.	48
4.3. A single fluctuating vesicle, exposed to $2 \mu\text{M}$ BefA. Each image is 2 seconds apart.	48

CHAPTER I

LIPIDS, MEMBRANES, AND VESICLES

1.1. Introduction

The earth is home to an astounding diversity of life. It has permeated the globe, adapting to the most extreme environments and filling the tightest niches. This ubiquity is made possible by the four billion years of development that has led to the complexity and variation that exists in living things. It is easy to wonder at the millions of species, each with unique properties that allow them to survive in disparate environments.

The complexity of living things is fascinating, but makes them a seemingly daunting object of study for a physicist. Physics often takes a reductionist approach, focusing not on the details of the most intricate or unique systems, but on the unifying principles and commonalities between them. This is evident in the hunt for fundamental particles, universal laws, or simple models. Applying the physicist's approach to biology is incredibly fruitful. The goal of a biophysicist is therefore to study the fundamental aspects of living beings, because perhaps the only things more surprising than the diversity of life are its commonalities. All living things use DNA to store information, much of which encodes for proteins made of the same amino acids, and whether the organism is an elephant, a Douglas fir, or a bacterium this process occurs within a cell, one separated from its neighbors and its environment by a lipid membrane.

These lipid membranes are one of the most important biological materials and are the focus of my dissertation. I have focused on furthering

our understanding of their properties with the hope of better understanding one of the fundamental aspects of living organisms. This understanding, while fascinating and worthwhile in its own right, can also play an important role in medical advances such as drug delivery – both the Moderna and Pfizer/BioNTech vaccines for COVID-19 use lipids to encapsulate mRNA and get it inside cells. Of particular interest in this work are the fluid properties of membranes as they play an important role in the physical rearrangement of proteins embedded in the membrane and therefore cellular dynamics.

This first chapter will cover some of the background of lipids and membranes necessary to understand the work that follows. The second chapter focuses on the hydrodynamic boundary conditions of a lipid membrane, in short, how a membrane interacts with the fluid it exists in. I describe my experiments characterizing the flow boundary conditions, which had never before been directly measured. This chapter includes previously published co-authored material. I will then discuss the fluidity of the membrane itself in chapter 3, assessing the accuracy of a method to measure membrane viscosity before applying it to a previously unmeasurable system. The fourth chapter discusses work done in collaboration with Karen Guillemin's lab examining the effect of the newly discovered bacterial protein, BefA, on membrane topology and rigidity. This chapter contains figures from unpublished co-authored material. The final chapter includes possible extensions of this work and concluding remarks.

1.2. Lipids

The term lipid is a very broad one, describing a wide range of large molecules that are amphipathic, having a hydrophilic region and a hydrophobic region.

These include fatty acids, sterols, detergents, and some vitamins. The lipids that are important in this work are the lipids that self assemble into bilayers, and in particular, phospholipids. In phospholipids, the hydrophobic part is made up of two long hydrocarbon (acyl) chain tails that are bound to a glycerol molecule which in turn connects them to the headgroup. This is the hydrophilic part and contains a phosphate group, giving phospholipids their name. While the phosphate is always present, there are many different headgroups that distinguish lipids. Phosphatidylcholine (PC) is one of the most studied and common in membranes, and the main headgroup used in this research. The many lipids that have PC headgroups are distinguished by the length and saturation of their acyl chains.

[2]

Every lipid has a full chemical name that uniquely identifies it, but as these are unwieldy it can be much clearer to use abbreviated versions. These will use the length of the carbon chain and the number of double bonds followed by the two letter abbreviation of the headgroup. For more information when double bonds are present the location of the double bond is given by a Δ position, the number of carbons away from the headgroup that the double bond occurs. The conformation of the carbon bonds can also be stated by including either a cis or trans. For example, 1,2-dioleoyl-sn-glycero-3-phosphocholine can also be written as 18:1 (Δ 9-Cis) PC, or even more simply DOPC. Compare this to a lipid that is identical except there is no double bond: 1,2-distearoyl-sn-glycero-3-phosphocholine, which can be written as 18:0 PC or DSPC. While every lipid used in this work will have two matching acyl chains, this is by no means necessary as evidenced by 1-palmitoyl-2-oleoyl-glycero-3-phosphocholine, or 16:0-18:1 PC, or POPC. A lipid with identical tails to DOPC but a different headgroup is 1,2-dioleoyl-sn-glycero-

3-phosphoethanolamine, or 18:1 PE, or DOPE. The chemical structure of each of these lipids is shown in Figure 1.1.

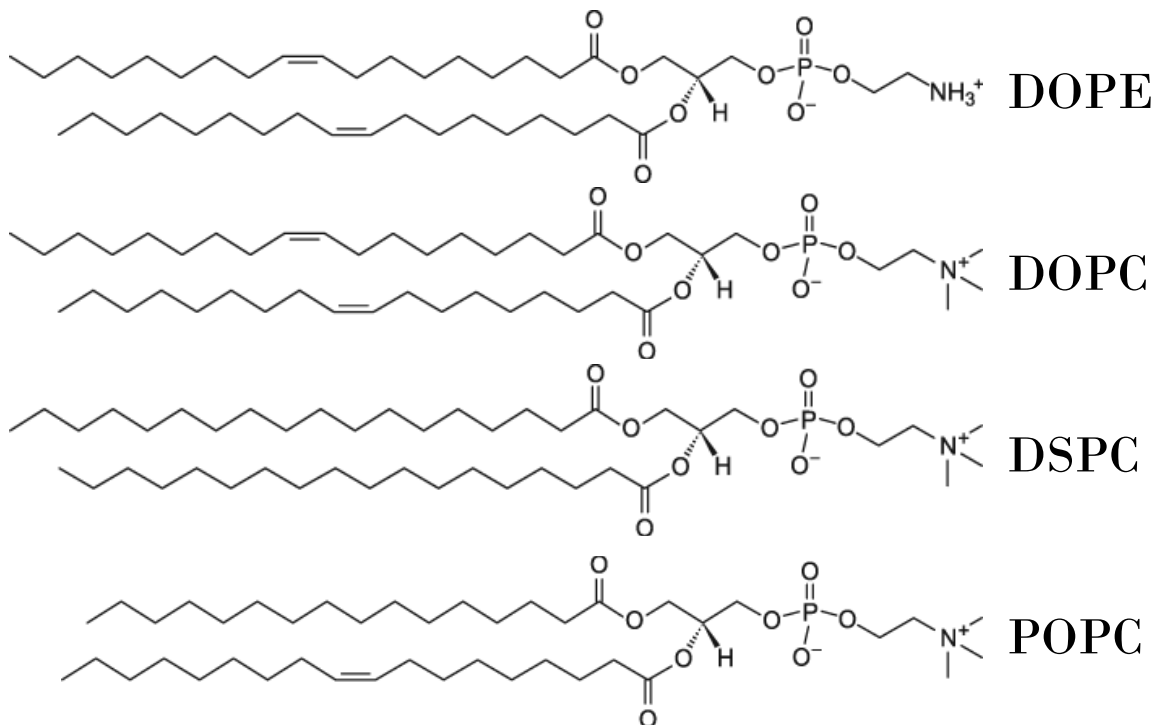


FIGURE 1.1. Bond line models of four example lipids, showing differences in head group, saturation, and chain length. Images taken from Avanti Lipids.

1.3. Membranes

Phospholipids are fairly simple molecules, but their amphipathic quality leads to interesting and powerful behavior. When exposed to water they self assemble into bilayers – sheets two molecules thick with the hydrophobic tails directed inwards, protected from the water by the hydrophilic heads on the outside. Even when only one lipid species is present, these bilayers can form several different phases: pseudocrystalline, gel, ripple, or liquid crystal. Depending on the chemistry of the specific lipid some phases will be unavailable, but some lipids, like DPPC (16:0 PC) can form all of them [3]. Phase transitions can be induced

by changes in temperature, pressure, tension, and hydration, but because of its comparative simplicity and more immediate applicability to most experiments, we will only focus on temperature.

At the lowest temperature, lipids will form the pseudocrystalline L_C phase with lipids densely packed, similar to the crystalline structure of non-hydrated lipids. The motion and rotation of the lipids are extremely limited in this phase. As temperature increases, the bilayer will enter the gel phase, L_β . In this phase, the headgroups are less tightly packed and arrange in a distorted orthorhombic lattice. The tails are tilted relative to the surface of the membrane. There is slightly more lipid rotation, but it is still largely restricted. Further increasing temperature leads to the ripple phase, P_β . The headgroups arrange in a hexagonal lattice and they displace vertically causing the membrane to form a “ripple”. This allows for nearly free rotation, but they remain limited in lateral mobility. [3]

The final transition is the most significant. At high enough temperatures the acyl chains, which were fully extended in all other phases, melt and are able to form both cis and trans bonds. This creates the liquid crystalline (L_α) or liquid disordered (L_D) phase. The relaxed hydrocarbon chains cause the membrane to expand laterally and thin as the lipids increase their cross sectional area and effectively shorten their carbon chains. This greatly increases the fluidity of the membrane, allowing for far greater lipid diffusion, orders of magnitude higher than in the gel phase [3]. Each phase is shown in Figure 1.2.

All of these phases occur in single species lipid membranes, but additions of other lipids can create additional phases and behaviors. The presence of cholesterol can cause an intermediary state between the gel and liquid disordered phases. While cholesterol itself will not form bilayers, it is nonetheless present

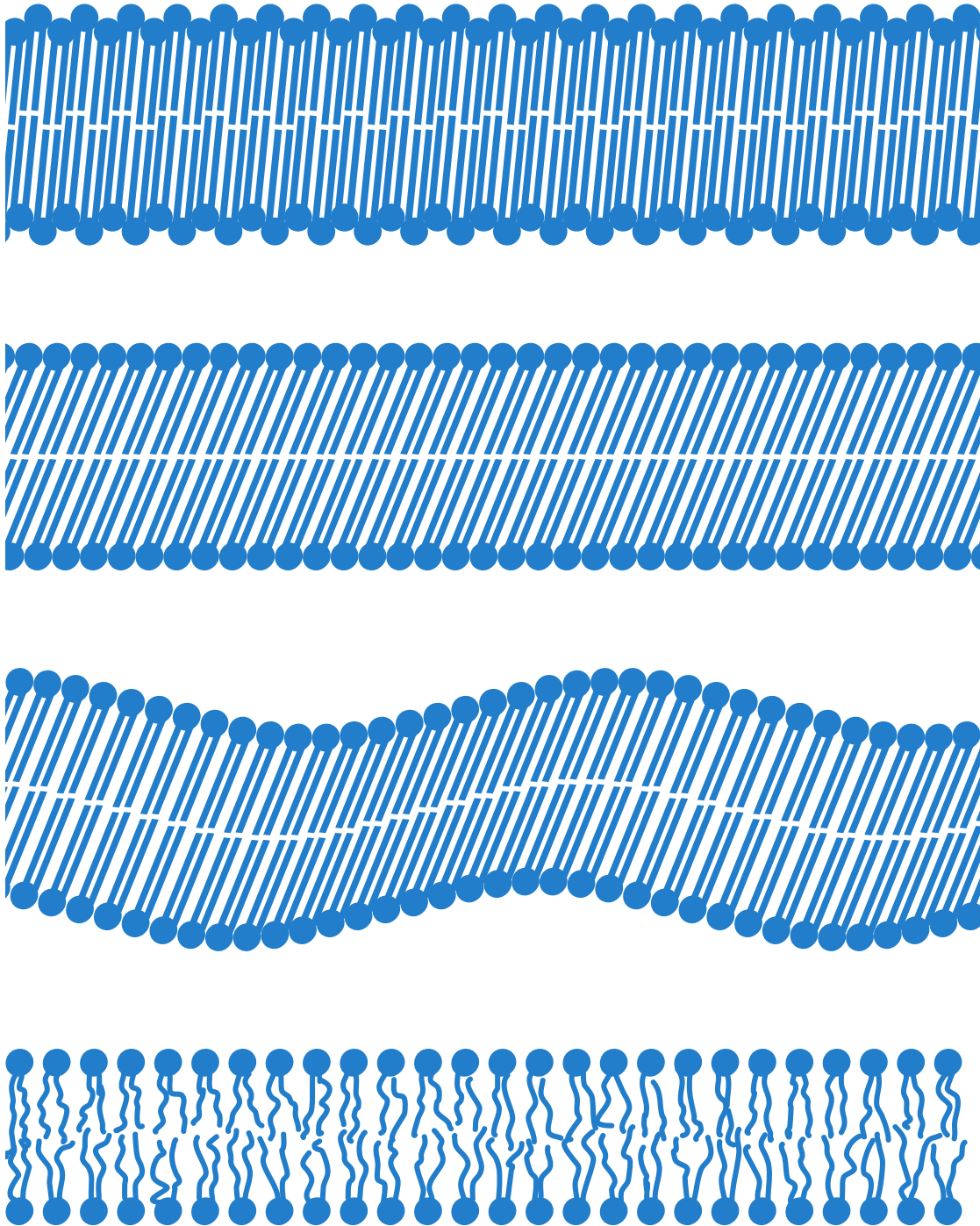


FIGURE 1.2. A schematic of the phases of lipid membranes – from the top, pseudocrystalline (L_C), gel (L_β), ripple (P_β), liquid disordered (L_D)

in high concentrations in animal membranes. Cholesterol is nearly entirely hydrophobic with only a single hydroxide group being hydrophilic. As such, it is fully embedded in the lipid bilayer and affects the behavior of the acyl chains above and below their melting temperature. Below the melting temperature, where the phospholipids would normally be in the gel phase, the cholesterol increases the spacing of the acyl chains, greatly increasing the fluidity. Above the melting temperature, the chains appear to be more ordered [3]. This results in the liquid ordered (L_O) fluid phase with lipid diffusion slightly below that of the liquid disordered phase [4]. This is shown in Figure 1.3.

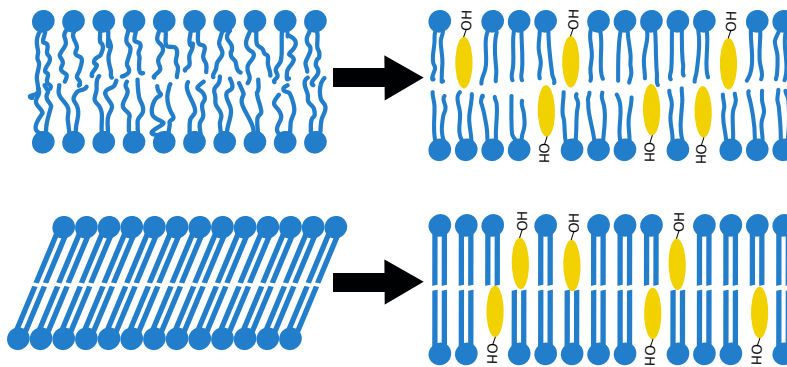


FIGURE 1.3. A schematic of the liquid ordered phase achieved by adding cholesterol when above the melting temperature (top) or below the melting temperature (bottom)

These two liquid phases, ordered and disordered, can coexist, and certain combinations of bilayer forming lipids with cholesterol will form clearly separated domains of different phases [5]. These large, micron scale phase domains do not occur for any single phospholipid combined with cholesterol, but will for a variety of phospholipid pairs with cholesterol [6]. These systems are a common area of study as a model for the somewhat controversial lipid rafts in living cells [7, 8], but also provide a unique method in which the diffusion of the domains is measured

in order to calculate the viscosity of the membrane [9, 10]. This will be further discussed and used in chapter 3.

1.4. Vesicles

In order to study lipid membranes, we take a reductionist approach using purified lipids to reconstitute membranes. The complexity of a cell membrane with proteins, cytoskeletal filaments and carbohydrates makes cellular membranes challenging to study. Fortunately, there are many methods for creating model lipid bilayers in vitro, allowing for control of the geometry and composition.

The different geometries each have their own advantages and uses. For example, supported lipid bilayers (SLBs), shown in Figure 1.4(a) are formed on a solid substrate, making them extremely stable [11] and allowing for techniques that require proximity to a solid surface like total internal reflection fluorescence microscopy [12]. However, this support is also its greatest limitation as it affects the behavior of the lipids, decreasing their diffusion [13].

Another commonly used system is the black lipid membrane (BLM) [14]. In this case, lipids dissolved in a hydrophobic solvent are painted across a circular aperture. This results in a lipid monolayer forming on either side of the solvent, shielding it from the water. As the solvent thins this becomes a planar bilayer that is only supported at the edges [15], as shown in Figure 1.4(b). Because there are large, separate aqueous solutions on either side of the bilayer, this makes it simple to perform electrical characterization of the membrane by inserting electrodes on either side, and it is even possible to insert ion channel proteins into the membrane [16, 17, 18]. It is possible for the solvent used to apply the lipids to not fully leave

the bilayer, leaving a thin layer of solvent between the leaflets which can affect the membrane behavior [19].

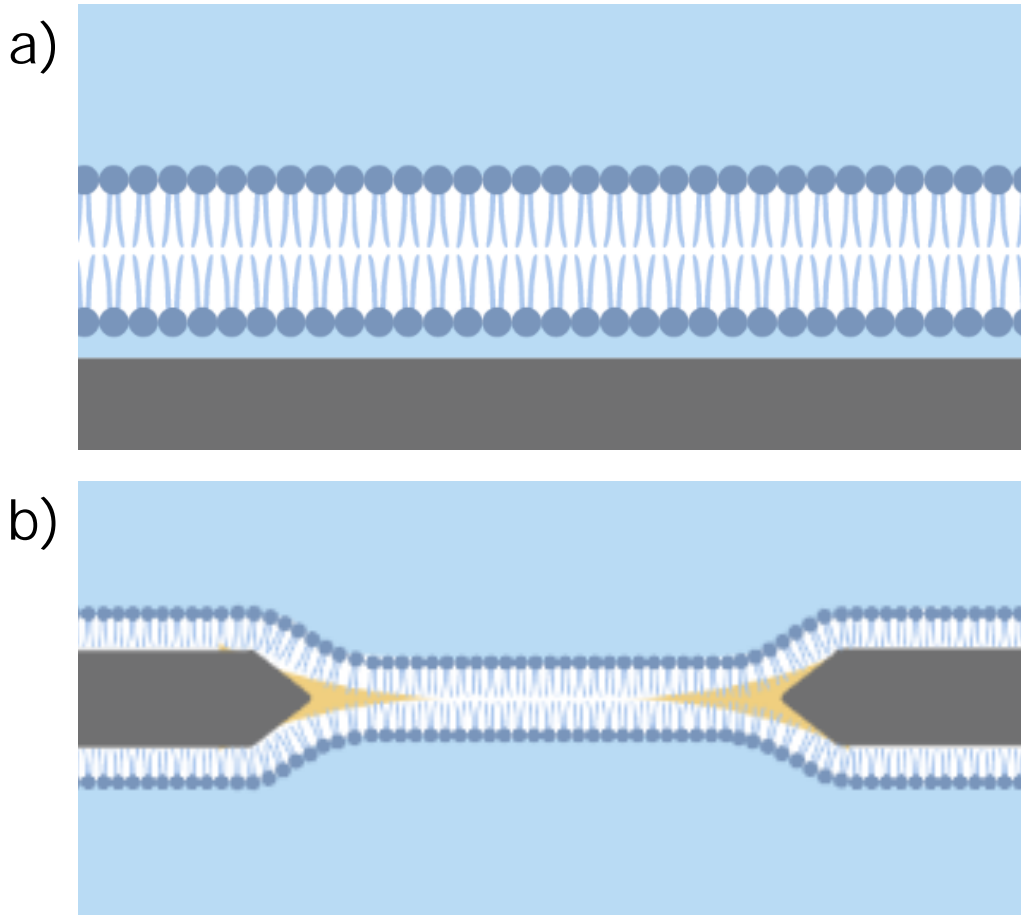


FIGURE 1.4. Top: A schematic of a supported lipid bilayer and Bottom: a black lipid membrane

In order to ensure nothing altered the lipid properties, all experiments performed in this work were performed using closed spherical bilayers, or vesicles. Unlike the previously mentioned planar structures, the lipid bilayer of a vesicle forms a spherical shell with fluid inside and out. This is structurally similar to natural lipid membranes like the cell membrane or naturally produced vesicles used for transport within a cell or between cells. They are also generally simple to create as they will spontaneously form when dried lipids are exposed to water.

While there is an energy cost to bending a membrane, any edges would expose the tails to water, so bilayers will naturally form vesicles. These can be many orders of magnitude larger than the width of the membrane: it is easy to make vesicles tens of microns in diameter, compared to a bilayer thickness of around 5nm. To illustrate this difference, if a vesicle $20\mu\text{m}$ in diameter were expanded to the size of an exercise ball, the membrane would be about as thick as a piece of paper.

While there are many methods for creating vesicles, such as various microfluidic techniques [20, 21], or even isolating vesicles from cell cultures [22, 23], the most common involve some variation on this spontaneous formation from hydration. Many of the vesicles created by simply exposing dried lipids to water will be multilamellar, with many layers inside of them. In order to achieve more consistent unilamellar vesicles, steps can be taken after or during the hydration process. Common techniques include sonication, placing hydrated lipids in a sonicator [24], and extrusion, forcing hydrated lipids through membranes with small pores [25]. Both of these result in vesicles too small for our purposes, with diameters only getting as large as a couple hundred nanometers. Vesicles of this size are challenging to study using traditional fluorescence microscopy as they are smaller than the wavelength of light.

Instead we used electroformation as described by Veatch et al. [26] to generate vesicles on the order of tens of microns. In this method, lipids of the desired composition dissolved in chloroform are deposited onto two sheets of indium tin oxide (ITO) coated glass and allowed to dry under vacuum. These are sandwiched together with a silicone spacer keeping them apart and sealing the edges. The cavity is filled with a sucrose solution and electrodes are attached to each sheet. By varying the voltage across the ITO glass sheets we create an

oscillating electric field in the cavity, promoting the formation of giant unilamellar vesicles, as shown in Figure 1.5. The details of how this process works remain poorly understood, but its simplicity and yield have made it commonplace in membrane biophysics research.

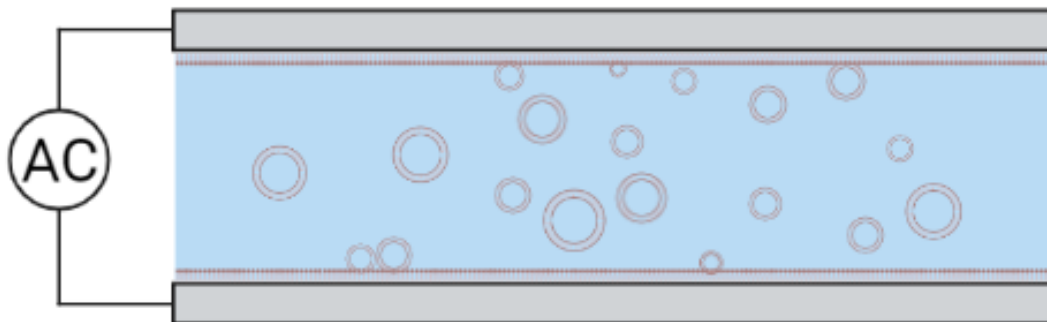


FIGURE 1.5. A schematic of vesicle creation using electroformation. Lipids deposited on ITO coated glass slides and a sucrose solution is placed between them. The slides are connected to an alternating voltage source, creating an oscillating electric field that encourages vesicle formation.

1.5. Conclusion

In this chapter, I have attempted to provide a brief but broad background of the chemistry and methods that underlie the work to come. I will provide additional background specific to particular experiments in each of the subsequent chapters. With the fundamentals of lipid chemistry, bilayer behavior, and bilayer formation covered we can move forward to studying the physics of the interaction of a free bilayer and the surrounding fluid environment.

CHAPTER II

LIPID BILAYER HYDRODYNAMIC DRAG

This chapter contains previously published co-authored material with contributions from Raghuveer Parthasarathy. In this work I contributed to designing the research, performing the research, analyzing the data, and writing the paper.

2.1. Introduction

Interfaces between lipid bilayers and aqueous solutions are present in countless environments both natural, such as at cell and organelle membranes, and artificial, such as in suspensions of liposome-encapsulated drugs. The hydrodynamics of bilayers and bilayer-bound objects are therefore of considerable interest [9, 20, 27, 28, 29, 30, 31, 32]. In particular, the rheology of red blood cells *in vivo* [33] and suspensions of cells and liposomes *in vitro* [34, 35] depends directly on the nature of the flow boundary condition of the bilayer / water interface. It has been widely assumed throughout work spanning many decades that this interface is well described by the boundary condition characteristic of a rigid solid [28, 36, 37, 38, 39, 40]. Experimental and computational studies of tracer particles flowing inside and outside lipid vesicles are consistent with this claim [41, 42, 43], but the complexity of the relationships between particle motions and membrane properties prohibit straightforward readouts. However, lipid bilayers are Newtonian fluids [9, 31, 44], and it has been speculated that their aqueous interfaces may therefore behave more like low-shear-stress boundaries, or have characteristics intermediate between inviscid and solid-like extremes [45]. For

bulk liquid droplets, intermediate shear conditions arise as internal fluid flows are directed in the opposite direction as drag-induced surface flows. Theoretically, therefore, an ideal spherical shell composed of an incompressible fluid would behave similarly to a rigid solid sphere, as the fluid cannot move to the interior space. The extent to which a real lipid vesicle behaves, in this sense, as an ideal spherical shell is experimentally unclear. One could imagine, for example, that differential flows between the two leaflets of the bilayer could allow relative tank-treading motions that reduce drag from the hard-sphere value. Molecular dynamics simulations often report finite shear at the bilayer-water interface (e.g. [29, 46]), and also give estimates of inter-leaflet slip [46]. One could alternatively imagine that thermally driven height fluctuations, even if too small to resolve, perceptibly increase drag.

Remarkably, despite its fundamental importance and widespread applicability, we are aware of almost no measurements of the hydrodynamic boundary conditions at lipid bilayer surfaces. One study was able to use a dynamic surface force apparatus to probe lipid bilayers supported on solid surfaces, reporting “no-slip” boundary conditions at the bilayer-water interface, as would be the case at a solid surface in water [47]. However, the presence of a solid support is well known to alter membrane hydrodynamics, reducing lipid diffusion by roughly an order of magnitude compared to free bilayers and inhibiting large-scale spatial organization [48, 49]. To the best of our knowledge, determining the flow boundary conditions at free lipid bilayers remains an open problem.

In principle, the interfacial boundary condition of an object can be determined from measurements of its Brownian Motion. For a sphere of radius

R , the diffusion coefficient D is given by the the Stokes-Einstein relation

$$D = \frac{k_B T}{C \pi \eta R}, \quad (2.1)$$

where k_B is Boltzmann's constant, T is the temperature, η is the external fluid viscosity, and C is a dimensionless constant that characterizes the boundary condition. It is well known that $C = 6$ corresponds to the limiting case of a rigid sphere, and $C = 4$ corresponds to an interface with no shear stress, as is the case for a liquid sphere of zero viscosity. More generally, for a sphere of viscosity η_{internal} in an external liquid of viscosity η_{external} , with

$$\lambda = \frac{\eta_{\text{internal}}}{\eta_{\text{external}}}, \quad (2.2)$$

the boundary constant is [50, 51, 52]:

$$C = 4 \frac{3\lambda + 2}{2\lambda + 2} \quad (2.3)$$

We note that determining C by measuring D does not provide insight into local flows that may occur at length-scales much smaller than the vesicle size or time-scales much shorter than attainable measurement times. Rather, it provides a characterization of the average, effective hydrodynamic properties of the vesicle.

In practice, determining C by measuring D is non-trivial due to potential hydrodynamic influence from nearby surfaces such as container walls, and the requirement of high-precision determination of the object's positions and radius.

We surmount these challenges by applying light sheet fluorescence microscopy [53, 54, 55, 56] together with fast, accurate tracking techniques [57]

to characterize the diffusive motion of spherical phospholipid vesicles. Light sheet fluorescence microscopy provides optical sectioning of three-dimensional samples, enabling the imaging of vesicles hundreds of microns (tens of vesicle diameters) away from the walls of the imaging chamber [54]. We verified our methodology by characterizing the diffusive motion of solid microspheres in an aqueous medium and water droplets in benzyl alcohol, as detailed below, which gives $C = 6.28 \pm 0.15$ and $C = 4.36 \pm 0.28$, respectively, consistent with theoretical expectations. We are therefore able to accurately measure the entire range of boundary behaviors. We then characterized lipid vesicles composed primarily of the common phospholipid DOPC (1,2-dioleoyl-sn-glycero-3-phosphocholine), determining that $C = 5.92 \pm 0.13$ (stat.) ± 0.16 (syst.). This establishes that the bilayer/water interface is well described by the interfacial shear stress condition of a solid object.

2.2. Methods

We performed light sheet fluorescence microscopy using a home-built instrument that closely follows the design of Keller et al. [56] and is described in detail in [55]. In brief, excitation light was provided by a 488 nm laser with an output power of 50 mW, which was scanned by a galvanometer mirror and focused by an objective lens to form a sheet in the sample chamber. The minimum thickness of the sheet was $\approx 3 \mu\text{m}$, extending over a lateral extent (Rayleigh length) of $\approx 100 \mu\text{m}$. Images were captured through a $40\times$ 1.0 NA Plan-apo objective lens (Zeiss) perpendicular to the excitation plane and recorded with a 5.5 Mpixel sCMOS camera (pco.edge, Cooke Corp.). A schematic of the setup is shown in Figure 2.1(a).

Suspensions of either lipid vesicles or polystyrene microspheres in 0.1 Molar sucrose, or deionized water droplets in benzyl alcohol, were placed in a square cross-section glass cuvette (Starna Cells, part number 3-3.45-SOG-3), which was mounted to a movable translation stage and inserted in the light sheet microscopy chamber. The distance between imaged objects and the cuvette walls was several hundred micrometers.

For beads, droplets, and vesicles the optical plane intersecting the sphere center (the “equatorial” plane) was readily evident due to a lack of out-of-focus light outside the bright ring or disk, due to the few micron sheet thickness. This is illustrated in Supplemental Movie 1, which shows a three-dimensional scan through a lipid vesicle.

To assess the accuracy of our methods, we examined diffusion of objects with well known flow boundary conditions: solid polystyrene microspheres and deionized water droplets suspended in benzyl alcohol.

The microspheres were FITC-labeled polystyrene beads of nominal diameter $15.45 \pm 0.70 \mu\text{m}$ (mean \pm standard deviation; Bangs Laboratory, part number FSDG009). Light sheet fluorescence images were captured for durations of 15 seconds at 33.33 frames per second. A typical image is shown in Figure 2.1(b). For the first image, we determine the particle center using the radial symmetry-based algorithm described in [57], which provides rapid localization with accuracy close to theoretical limits. In brief, the center is calculated as the point that minimizes total distance to lines derived from intensity gradients throughout the image. The original algorithm was modified to only weight intensity gradients from the vicinity of the bead, limiting the effects of noise outside the particle, such as fluorescent debris or light from other beads. Each remaining image was

cross correlated with the previous image and the original radial symmetry-based algorithm was applied to the cross-correlation to determine the shift between each frame. From the particle positions, we determine the diffusion coefficient D using the covariance based estimator described by Vestergaard et. al. [58]. Not only does this provide greater accuracy than, for example, linear fits of mean-squared-displacements to time intervals, but it also provides robust estimates of localization accuracy and goodness-of-fit to a random walk model [58] that we make use of in assessing vesicle data below. We experimentally determined the radius of each bead by Hough transformation following edge detection [59], which produces from each input image a series of output images corresponding to each possible radius candidate, with the true object radius giving a bright, compact transform image. Across all beads, this gives an average diameter of $15.06 \pm 0.41 \mu\text{m}$ (mean \pm standard deviation), consistent with the nominal value of $15.45 \pm 0.70 \mu\text{m}$. Using the measured radius, the literature value for the viscosity of deionized water, and the ambient temperature $T = 293 \text{ K}$, we use Eq. 2.1 to determine C for each microsphere. We show the histogram of C values for $N = 29$ microspheres in Figure 2.1(b). The mean \pm standard error is $C = 6.28 \pm 0.15$, slightly higher than but consistent with the expected $C = 6$ for solid particles. (Using the nominal rather than the measured microsphere radius gives $C = 6.12$, matching the theoretical value within uncertainties. The microsphere edges are less well-defined than those of the vesicles; in the latter case, we note explicitly the uncertainty in R below.)

The assessment of liquid droplets is similar. The droplets were deionized water dyed with 75 mg/ml fluorescein, suspended in benzyl alcohol, formed into an emulsion by vigorous shaking. Fluorescein has very low solubility in water, but

nonetheless preferentially labels the aqueous phase. Benzyl alcohol was chosen because its density, 1.045 g/ml, is similar to that of water, limiting gravity-induced drift. The viscosity of benzyl alcohol is $\eta = 6.29 \times 10^{-3}$ Pa·s [60], and so the expected $C = 4.27$. The droplets were imaged for 60 seconds at 8.33 frames per second. A typical image is shown in Figure 2.1(c). Using the same procedures described above for center positions and radii, we determined C for each water droplet. Figure 2.1(d) shows the histogram of C values for $N = 25$ droplets. The mean \pm standard error is $C = 4.36 \pm 0.29$, consistent with the expected value. Notably, C increased with time for these droplets, likely due to adsorption of fluorescein to the boundary as the poorly soluble dye lowers the oil/water interfacial energy. With sufficient adsorption, the droplet properties are those of an oil/fluorescein rather than an oil/water interface and may reflect possible ordering of a fluorescein monolayer or pure monolayer hydrodynamics. The C value stated was determined from data within 20 minutes of emulsion preparation.

The lipid vesicles we examined were composed of 94% DOPC (1,2-dioleoyl-sn-glycero-3-phosphocholine), and 6% NBD-PE (1,2-dipalmitoyl-sn-glycerco-3-phosphoethanolamine-N-(7-nitro-2-1,3-benzoxadiazol-4-yl) (Avanti Polar Lipids). Phosphatidylcholine lipids are a major constituent of cellular membranes. The headgroup-conjugated NBD probe has an isotropic orientation relative to the lipid bilayer plane (unlike, for example, probes such as Texas Red [61]), and so provides vesicle images of symmetric fluorescence under polarized laser excitation. The vesicles had radii between 3.1 and 25.7 μm with a mean of 12.2 μm and a standard deviation of 4.0 μm . Vesicles were imaged for 15 seconds at 33.33 frames per second. The vesicles were created by electroformation, as in [26]. In brief, the desired lipids were dried on glass slides with an indium tin oxide coating, hydrated

with a 0.1 M sucrose solution, and subjected to an oscillating electric field to stimulate vesicle formation. Vesicles were added to a sample cuvette containing 0.1 M sucrose so that the interior and exterior of the vesicles would be matched in density and osmolarity. We use the literature value for the viscosity of 0.1 M sucrose, $\eta = 1.095 \times 10^{-3}$ Pa·s [62], in our analyses. Low levels of drift were present in the experiments, possibly due to convection and imperfect density matching. We therefore subtracted the best-fit linear trajectory (i.e. constant velocity) from each vesicle trajectory, and used only the horizontal component of trajectories. Rare frame-to-frame displacements more than three standard deviations from the mean ($< 0.5\%$ of frames) appeared to indicate large-scale instrument vibrations, and trajectories were analyzed piecewise around such points.

We assessed the accuracy of center- and radius-finding algorithms for vesicle images by applying them to simulated images of bright rings with a range of radii and signal-to-noise ratios (SNRs), mimicking the form of the vesicle images, as in Ref. [54] and similar to the ring images in Ref. [57]. In brief, a high-resolution image of a thin annulus was convolved with the detection point-spread function (PSF), pixelated, and subjected to Poisson-distributed noise. We used the theoretical PSF of the emission wavelength and numerical aperture, which has a full-width at half-maximum of $0.19 \mu\text{m}$. Because of the occasional presence of lipid matter in and around the vesicle edge, the radial center-finding algorithm is weighted with a hyperbolic tangent function centered around the ring of the vesicle so as to only use the intensity gradient from the edge of the vesicle. From analysis of simulated images, the radial-symmetry-based localization gives an estimated localization error of ≈ 3 nm. Independently, the localization error estimated from vesicle trajectories by the method of Vestergaard et al.[58] is ≈ 10 nm. The vesicle

radius is determined by Hough transformation, as in the bead and droplet image analysis. The estimated uncertainty in R from the standard deviation of simulated images at the appropriate SNR is $\approx 0.005 \mu\text{m}$. More significant, however, is the standard deviation in R over the course of an image series, due for example to changes in position relative to the sheet plane. This is $\approx 0.03 \mu\text{m}$, which is small compared to the typical $10 \mu\text{m}$ vesicle radii and which contributes negligibly to the overall uncertainty in C . From vesicle position data, we calculated D and C as described above.

2.3. Results

Light sheet fluorescence microscopy provides clear images of lipid vesicles. A typical example is shown in Figure 2.2(a). Assessment of images as described above provides vesicle positions, radii, diffusion coefficients (D), and the flow boundary constant (C), along with their uncertainties. We provide the complete set of positions, radii, diffusion coefficients, and boundary coefficient values for every microsphere, water droplet, and lipid vesicle examined as Supplemental File.

In Figure 2.2(b) we show ten randomly chosen examples of vesicle mean-squared-displacement(MSD) (colored lines) as a function of lag time together with their average (dashed gray line). The linearity of the MSD curve is indicative of free diffusion. A more robust assessment of the Brownian character of vesicle motion comes from the goodness of fit calculation provided by the covariance based estimator of D , which gives a reduced χ^2 value whose value should be ≈ 1 for a model of pure diffusion. A histogram of the measured χ^2 values is shown in Figure 2.2(c), and is consistent with simple Brownian diffusion.

As described in Methods, we use measurements of vesicle radii and diffusion coefficients to determine the flow boundary condition constant C . The histogram of C for $N = 26$ vesicles is shown in Figure 2.2(d). The mean \pm standard error is $C = 5.92 \pm 0.13$. To estimate possible systematic error, we assume that the polystyrene microspheres for which we calculated C (see Methods) are ideal hard spheres. The standard deviation of the beads' C value would therefore be the spread inherent in our methodology. In order to account for this uncertainty we can compute a systematic standard error by dividing the standard deviation of the beads' C by the square root of the number of vesicles. This gives us a constant for vesicles of $C = 5.92 \pm 0.13$ (stat.) ± 0.16 (syst.).

Our measurements show that at least over micrometer length scales and millisecond-to-second timescales, lipid bilayers are well described by the shear stress boundary conditions that characterize solid surfaces in fluid. Perhaps reassuringly, the standard assumption that is ubiquitous in treatments of liposome hydrodynamics is well supported.

Our method illustrates that a conceptually simple imaging-based approach can provide precision measurements of microscale fluid properties. We expect that this can be extended to, for example, fluctuating membranes driven by either temperature [54, 63] or active forces [64] to investigate couplings between topography and drag. Put differently, the precision with which the value $C = 6$ can be determined, even if one views the value itself as an unsurprising confirmation of expectations, illuminates the precision that future studies of more exotic membrane systems can achieve. Finally, we note that the methods presented here will also be applicable in non-Newtonian fluids, for which detailed understanding of microscale rheology continues to be an active area of study.

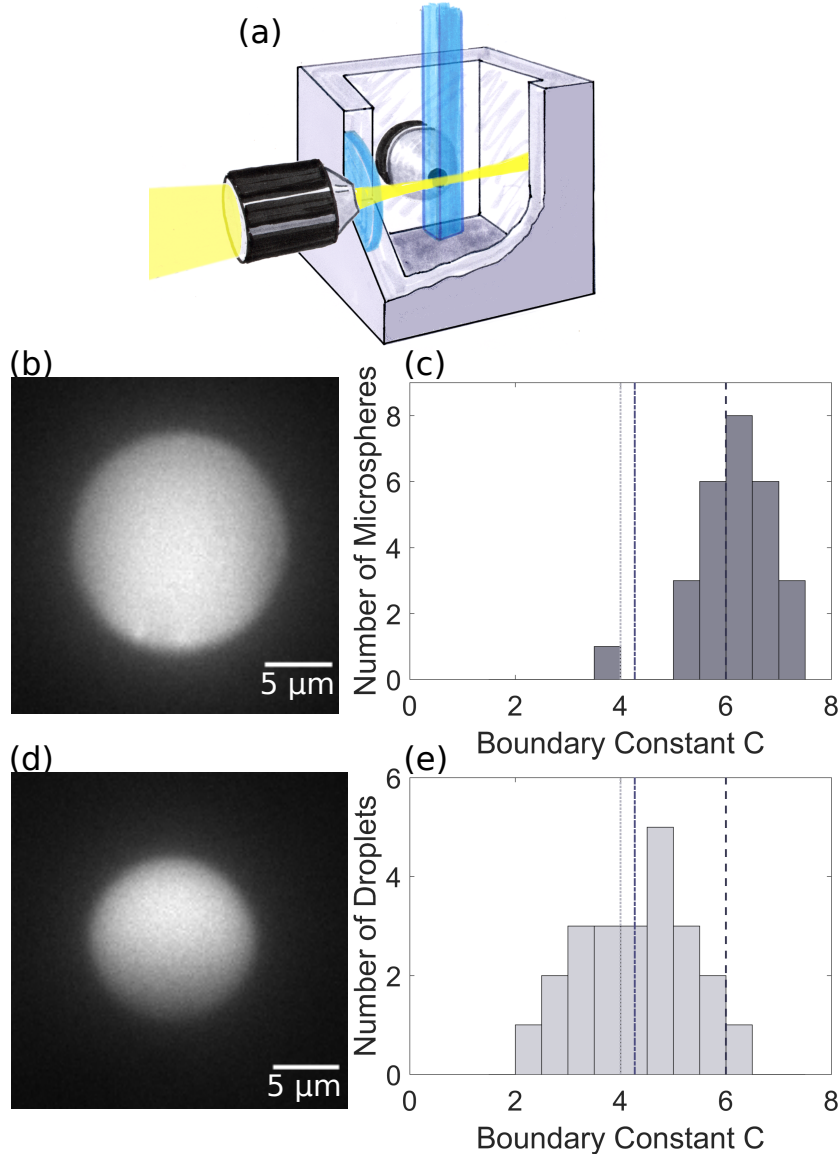


FIGURE 2.1. (a) A schematic of the setup for light sheet fluorescence microscopy of vesicle diffusion. The excitation laser is shown entering the sample chamber from the left as it is focused into a thin sheet. Light emitted by the sample is collected by the objective lens shown behind the cuvette. (b) A typical light sheet fluorescence image of the central plane of a $15\ \mu\text{m}$ diameter polystyrene microsphere. (c) Histogram of C for 29 particles, giving a mean \pm standard error of $C = 6.28 \pm 0.15$. (d) A typical light sheet fluorescence image of the central plane of a fluorescein-dyed water droplet in benzyl alcohol. (e) Histogram of C values for 25 droplets, giving a mean \pm standard error of $C = 4.36 \pm 0.29$. In (b) and (d), the dashed-dotted line indicates the theoretical value of $C = 4.27$ for water in benzyl alcohol and the dashed and dotted lines respectively indicate the theoretical values of $C = 6$ and $C = 4$ for the boundary conditions of a rigid sphere and an inviscid (zero shear stress) sphere.

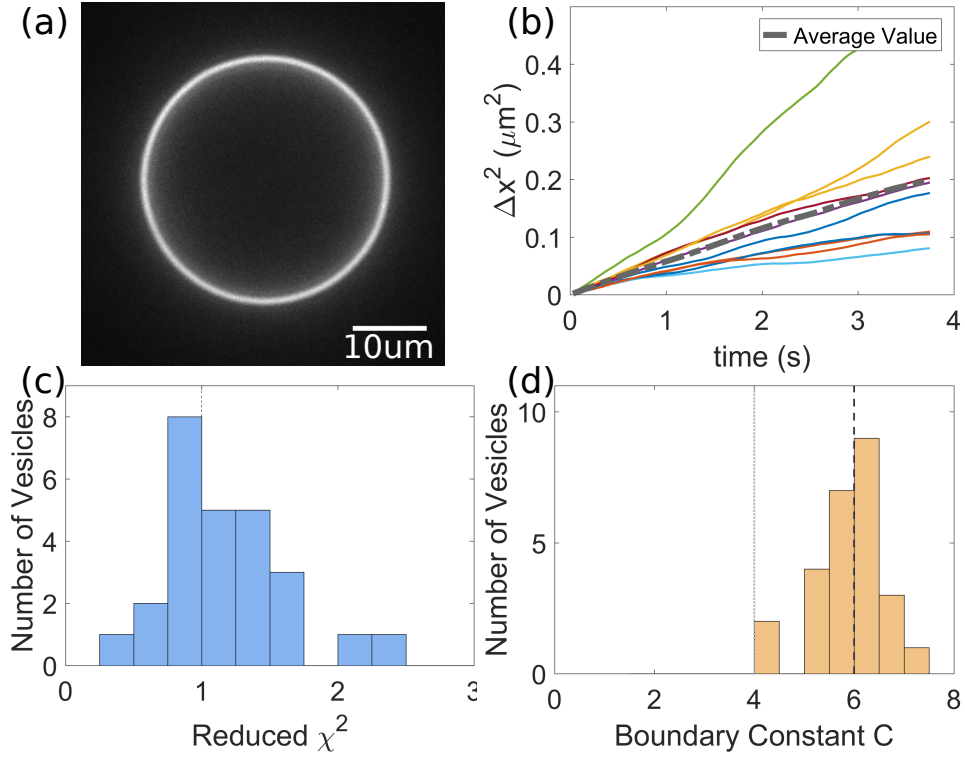


FIGURE 2.2. (a) A typical light sheet fluorescence image of the central plane of a DOPC vesicle. (b) Mean-square-displacements from 10 randomly chosen vesicle trajectories (colored lines), along with their average (dashed gray line). (c) Histogram of the reduced χ^2 values for each vesicle; $\chi^2 = 1$ indicates purely diffusive motion. (d) Histogram of C for 26 vesicles giving a mean \pm standard error of $C = 5.92 \pm 0.13$. The dashed and dotted lines indicate the theoretical values of $C = 6$ and $C = 4$ for the boundary conditions of a rigid sphere and an inviscid (zero shear stress) sphere.

CHAPTER III

COMPARISON OF MICRORHEOLOGICAL METHODS FOR MEASURING LIPID MEMBRANE VISCOSITY

3.1. Introduction

Cellular function is heavily dependent on the fluidity of lipid membranes, allowing proteins, macromolecules, lipid domains, and the lipids to self-organize into assemblies [9, 10, 65, 66, 67, 68]. The viscosity of the membrane sets the timescale at which these dynamics occur and so an accurate understanding is required to understand and predict their behavior. But despite measurements of lipid and protein diffusion being made regularly, it is not simple to use these to determine the viscosity. Part of the difficulty stems from the effect that the diffusing object has on the membrane. The effective radius of a protein or other tracer particle embedded in or attached to the membrane is not clear as it could be defined by a small binding site or by a large induced curvature, as shown in Figure 3.1.



FIGURE 3.1. A schematic of beads bound to a membrane. It is not obvious if the effective radius is small, as on the left where there is a small binding site, or large, as on the right where there is a large induced curvature.

Methods exist to address this issue. As in [9, 31, 32, 41, 44] phase separated domains can be used as tracers, as shown in Figure 3.2. Because these regions of distinct lipid phase are a part of the membrane itself rather than affixed to it, the radius of the domain can be taken as the effective radius. Alternatively, as in [30], elliptical tracer particles can be used. While the effective radius is unknown, by using both translational and rotational diffusion coefficients the viscosity, η , and radius can both be determined, as detailed below. This technique has the advantage of being applicable to a wide range of lipid systems, only requiring a low concentration of lipids that the particles are able to bind to, while using phase separated domains requires multiple lipid species and specific compositions that undergo phase separation.

Measurements of viscosity of phase separated vesicles have been performed by several groups and returned consistent values. For example, work done in our lab found $\eta = 0.75 \pm 0.15 \times 10^{-9} \text{ Pa} \cdot \text{s} \cdot \text{m}$ for the DOPC enriched liquid-disordered phase of phase separated vesicles [31], in close agreement with other labs' measurements [41, 44]. However, this is more than an order of magnitude smaller than the viscosity measured using non-spherical tracer particles for nearly pure DOPC membranes, $\eta = 15.9 \pm 2.3 \times 10^{-9} \text{ Pa} \cdot \text{s} \cdot \text{m}$, the only study to date using non-spherical tracers. This is a large discrepancy, even when considering the other lipids present in the L_D phase. It is most likely caused by residual solvent left between the leaflets of the black lipid membrane. It should be noted that the non-spherical tracers used in [31] were pairs of beads, one coated with neutravidin and the other with biotin. The lipid membrane included biotinylated lipids so that only the neutravidin coated bead would bind to the membrane. When imaging a pair of bound beads would appear as a single extended body enabling the

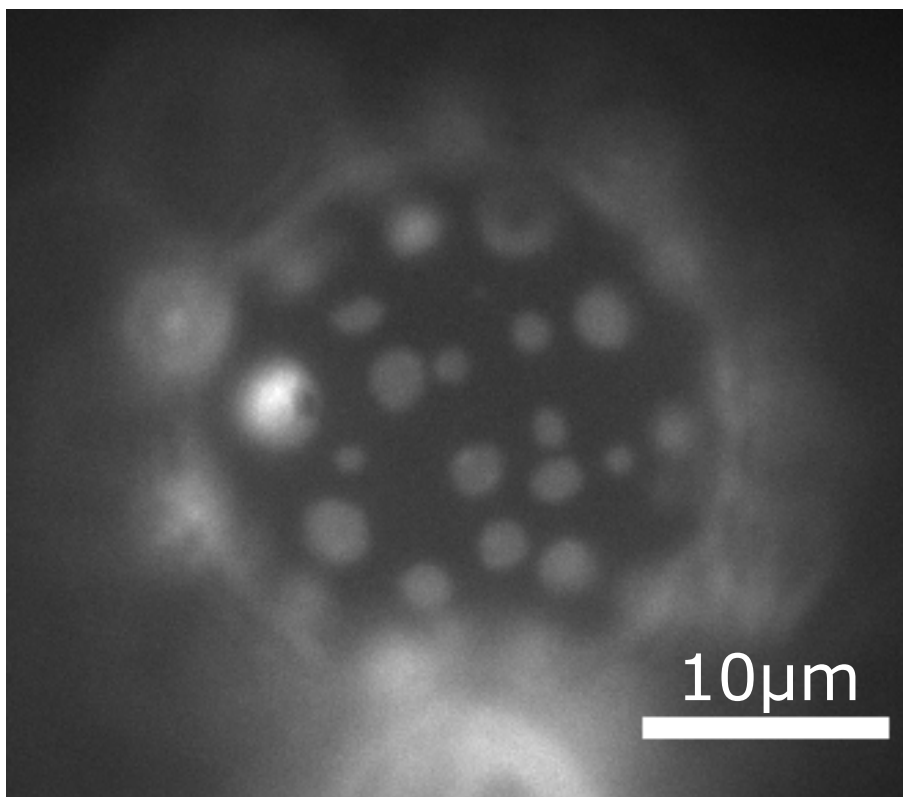


FIGURE 3.2. An example image of the pole of a vesicle that has undergone phase separation with bright liquid-disordered domains in the main liquid-ordered phase. Imaged at room temperature, and comprised of DPPC, DOPC,Cholesterol, DOTAP, 16:0 Biotinyl PE, and Texas Red DHPE

measurement of the rotational motion while behaving as a rotationally symmetric circular inclusion. In order to simplify the binding and preparation process, we use elliptical beads as the non-spherical tracers. These are not necessarily rotationally symmetric circular inclusions and so will require a different analysis, described below. A schematic of both methods is shown in Figure 3.3.

To resolve the discrepancy and assess the accuracy of the determination of membrane viscosity using non-spherical tracers, we apply the method on phase separated vesicles, measuring viscosity from elliptical beads and domains simultaneously, the first direct comparison of the methods.

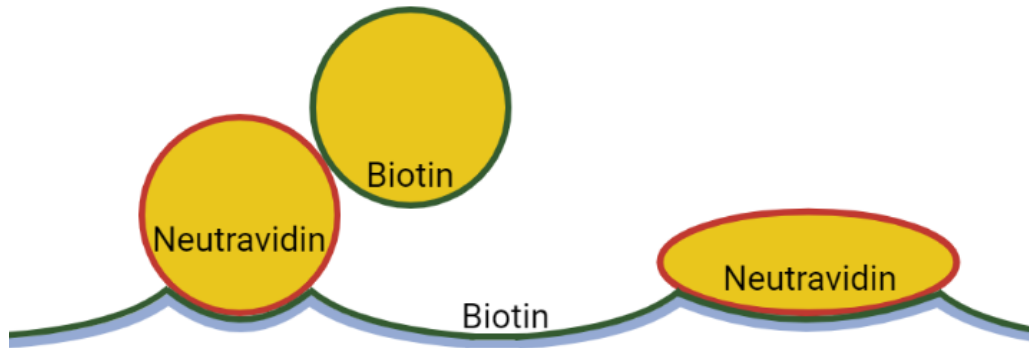


FIGURE 3.3. On the left, a pair of beads form a non-spherical tracer. A membrane containing biotin binds to a neutravidin coated bead, which in turn is bound to a biotin coated bead. On the right, a single elliptical bead coated with neutravidin binds to the membrane, but does not form a circular inclusion.

3.2. Experimental Methods

A lipid concentration to form phase separated vesicles was chosen based on [6], but with modifications made in order ensure that beads bind. We used 35.5% DPPC (1,2-dipalmitoyl-sn-glycero-3-phosphocholine), 15.5% DOPC (1,2-dioleoyl-sn-glycero-3-phosphocholine), 40% Cholesterol, 8% DOTAP (1,2-dioleoyl-3-trimethylammonium-propane (chloride salt)), 0.5% 16:0 Biotinyl PE (1,2-dipalmitoyl-sn-glycero-3-phosphoethanolamine-N-(biotinyl) (sodium salt)), and 0.5% Texas Red DHPE (1,2-Dihexadecanoyl-sn-glycero-3-Phosphoethanolamine, Triethylammonium Salt). The Texas Red DHPE was purchased from ThermoFisher Scientific and all other lipids were purchased from Avanti Polar Lipids. This concentration of lipids will produce liquid-disordered (L_D) domains in a liquid-ordered (L_O) main phase. The fluorescently tagged Texas Red DHPE preferentially partitions into the L_D phase resulting in bright domains. The streptavidin coated beads strongly bind to the Biotinylated PE lipids. All vesicles were created using electroformation, as described in [26]. The lipids of

interest were deposited on indium tin oxide coated glass slides and dried before hydrating in 0.1M sucrose in an oscillating electric field.

Elliptical polystyrene beads were formed based on the method described in [69]. In short, 1 μm spherical polystyrene beads (Invitrogen catalog number F8776) were placed in a solution of 6.2% polyvinyl alcohol and 2.5% glycerol by mass in deionized water which was allowed to evaporate, leaving the beads embedded in a thin, flexible sheet. This sheet was placed in a mechanical stretching device as shown in Figure 3.4. But before extending the device, the film was submerged overnight in toluene, which dissolves the polystyrene beads without affecting the sheet. The sheet is then stretched and removed from the toluene allowing the particles to solidify in the shape of the now deformed cavities. Once the beads have solidified in the stretched film, the film can be dissolved in water and the beads are isolated with a centrifuge. Prior to use, the beads are soaked overnight in a 0.01 g/ml streptavidin solution in order to ensure binding to the biotinylated lipids in the vesicles. The beads are centrifuged and removed from the streptavidin solution and sonicated to break up any clumps. They are added to vesicles suspended in sucrose an hour before imaging to allow time for binding.

All images were recorded at 20 frames per second on a Nikon TE2000 inverted fluorescence microscope with a 60 \times oil immersion objective and a Hamamatsu Orca CCD camera at room temperature. A Cairn OptoSplit was used to simultaneously record two color channels, one for the domains and one for the beads.

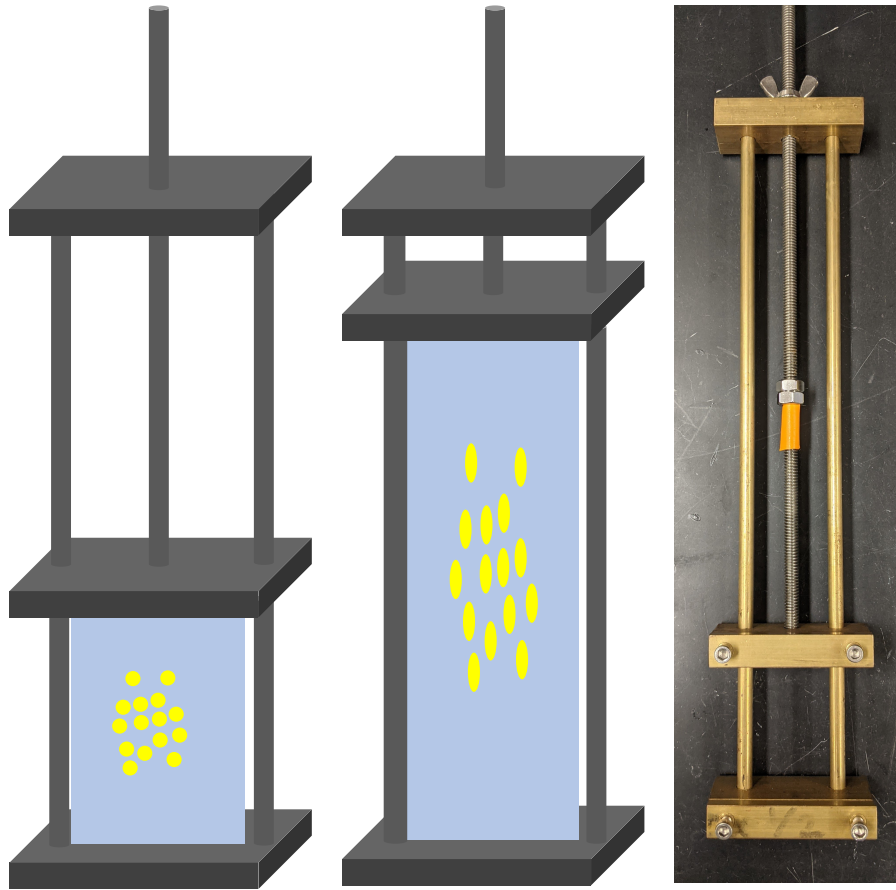


FIGURE 3.4. A schematic of the device used for stretching beads, before and after stretching, with the actual device.

3.3. Image Analysis

The analysis of phase separated domains follows the method described in [31]. Domains were identified with intensity thresholding and their centers were found by fitting Gaussian profiles using maximum likelihood estimation. The boundaries of domains were found with a bilateral filter and the area of each domain was used to determine the radius. Domain positions across frames were assigned to tracks by performing a nearest neighbor linking, only keeping time series for domains that were tracked continuously for at least 100 frames to ensure sufficient statistics to accurately calculate their diffusion coefficients.

Beads were detected by identifying the brightest single object in each frame and the centers were found using the radial symmetry-based algorithm described in [57], a rapid localization method with accuracy close to theoretical limits. The center is the point that minimizes the total distance from lines along intensity gradients throughout the image. The angle of the bead is found using the center as the starting point for fitting an ellipse to the image by determining the ellipsoid that matches the covariance matrix of the intensity.

The accuracy of this localization method was determined by applying it to simulated images of bright ellipses that mimic the size and signal-to-noise ratio of our data. A high-resolution image of an ellipse was convolved with the detection point-spread function based on the emission wavelength and numerical aperture, pixelated, and subjected to Poisson distributed noise. The center is found with a variance of ≈ 35 nm, well below the pixel size of 110 nm. The variance of the bead's angle was $\approx 0.25^\circ$.

Diffusion coefficients for domains and beads were determined using the covariance based method described by Vestergaard et al. [58]. This method provides greater accuracy than linear fits of mean-square displacements and provides estimates of localization accuracy and goodness of fit to a random walk.

3.4. Mathematical Analysis

The membranes formed by lipids can be many orders of magnitude larger than the thickness of the membrane, which is on the order of 5nm. This allows the membrane to be treated as a two dimensional fluid where the individual lipid molecules freely flow and diffuse within the membrane, but are confined to the thin sheet. This forms the basis of the models we use of membrane fluidity. In

1975 Saffman and Delbrück put forward a model for the diffusion of a cylinder in a two dimensional fluid bounded on either side by a bulk fluid [70]. They found that by accounting for the behavior of the membrane and the surrounding fluid the translational diffusion is given by

$$D_T = \frac{k_B T}{4\pi\eta} \left(\log \frac{\eta}{\eta_w a} - \gamma \right) \quad (3.1)$$

and the rotational diffusion is given by

$$D_R = \frac{k_B T}{4\pi\eta a^2} \quad (3.2)$$

where η is the two dimensional viscosity of the membrane, η_w is the viscosity of the surrounding fluid, a is the radius of the cylinder, and γ is Euler's constant. However, this method can only be applied only when the useful dimensionless quantity $\epsilon = \frac{2\eta_w a}{\eta} \ll 1$, i.e. systems where the membrane inclusion is small and the viscosity is large. This holds in lipid membranes for nano-scale objects, but will fail for micrometer scale lipid domains or particles. Hughes, Pailthorpe, and White (HPW) extended this model to arbitrary ϵ [71]. The HPW model is substantially more complicated and cannot be expressed in simple closed-form equations. Petrov and Schuille provide a simple analytical approximation that fits the full HPW model across all ϵ [44]:

$$D_T = \frac{k_B T}{4\pi\eta} \left[\ln \left(\frac{2}{\epsilon} \right) - \gamma + \frac{4\epsilon}{\pi} - \left(\frac{\epsilon^2}{2} \right) \ln \left(\frac{2}{\epsilon} \right) \right] \left[1 - \left(\frac{\epsilon^3}{\pi} \right) \ln \left(\frac{2}{\epsilon} \right) + \beta(\epsilon, b_{T1}, b_{T2}, c_{T1}, c_{T2}) \right]^{-1} \quad (3.3)$$

is the translational diffusion, where

$$\beta(\epsilon, b_{T1}, b_{T2}, c_{T1}, c_{T2}) = \frac{c_{T1}\epsilon^{b_{T1}}}{1 + c_{T2}\epsilon^{b_{T2}}} \quad (3.4)$$

and $b_{T1} = 2.74819$, $b_{T2} = 0.51465$, $c_{T1} = 0.73761$, and $c_{T2} = 0.52119$. The rotational diffusion is given by

$$D_R = \frac{(2\eta_w)^2}{4\pi\eta^3} \left[\epsilon^2 + \frac{4\epsilon^3}{3\pi} + \beta(\epsilon, b_{R1}, b_{R2}, c_{R1}, c_{R2}) \right]^{-1} \quad (3.5)$$

where β is the same function as in equation 3.4, but the constant values are given by $b_{R1} = 2.91587$, $b_{R2} = 0.68319$, $c_{R1} = 0.31943$, and $c_{R2} = 0.60737$.

The full HPW model and the Petrov-Schwille approximation have been shown to apply to phase separated domains [31, 44]. It should be noted that this model is for the diffusion of a circular inclusion in the membrane. As such, it is not clear that it can be applied to the motion of the elliptical beads. An elliptical bead may induce a roughly circular curvature or be bound to the membrane in only a small region, but there is no guarantee it will bind in a spherically symmetric way. If we plot curves of constant viscosity in rotational and translational diffusion coefficient space, as in Figure 3.5, we see that the low viscosities asymptote. Several of the measured translational and rotational diffusion coefficients of the elliptical beads fall beyond this asymptote in a disallowed region that does not correspond to any viscosity. In order to describe the motion of our elliptical beads we use the work of Levine, Liverpool, and MacKintosh (LLM) on the motion of extended bodies in membranes [72]. They give the rotational diffusion

$$D_R = \frac{1}{c_R(\lambda)} \frac{k_B T}{4\pi\eta L^2} \quad (3.6)$$

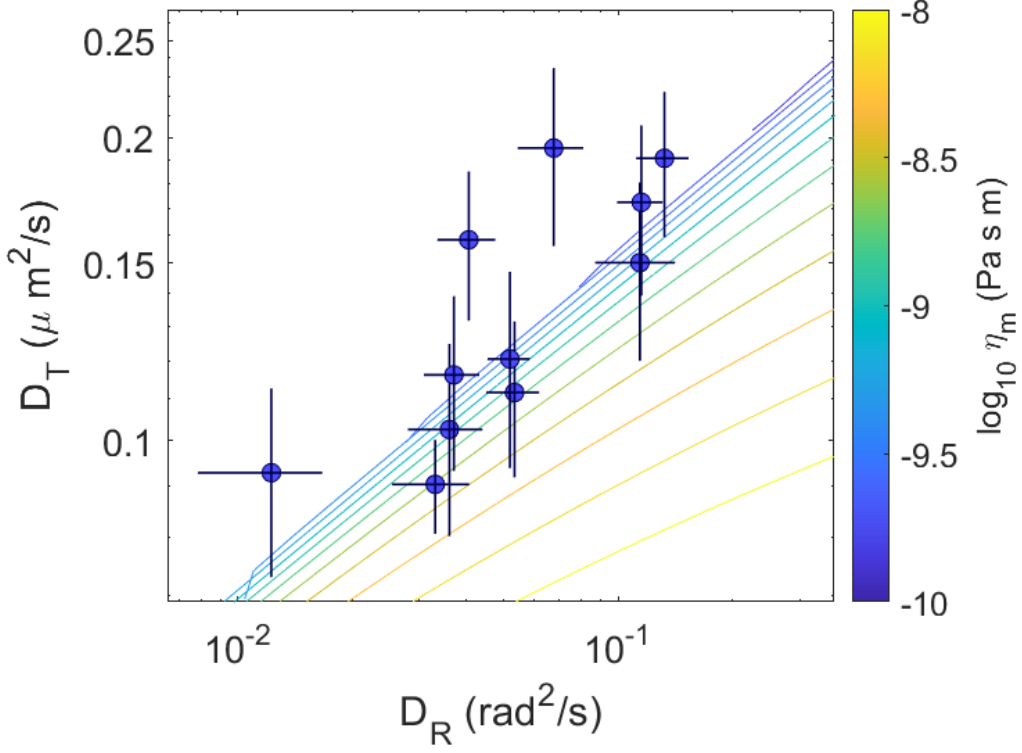


FIGURE 3.5. Translational diffusion coefficient vs. the rotational diffusion coefficient with curves of constant viscosity based on the HPW model. Many of the points fall outside the allowed region because the inclusions are not rotationally symmetric.

where L is the length of the rod and c_R is a function that depends on $\lambda = \frac{2\eta_w L}{\eta}$. In this case, λ is a dimensionless variable analogous to the ϵ used in the SD and HPW models. Because the translational diffusion of an elliptical object will depend on its orientation, Levine provides expressions for the diffusion along the axes parallel and perpendicular to the extended body's long axis. These are

$$D_{\perp} = \frac{1}{c_{\perp}(\lambda)} \frac{k_B T}{4\pi\eta} \quad (3.7)$$

$$D_{\parallel} = \frac{1}{c_{\parallel}(\lambda)} \frac{k_B T}{4\pi\eta} \quad (3.8)$$

The functions that define the coefficients in each of these equations are taken from [72], but they are not provided explicitly. We fit a curve to the plots in order to solve for viscosity and effective bead length analytically. These fits were compared to values provided by the authors to ensure accuracy. Our data falls into the allowed regime of this theory, shown in Figure 3.6.

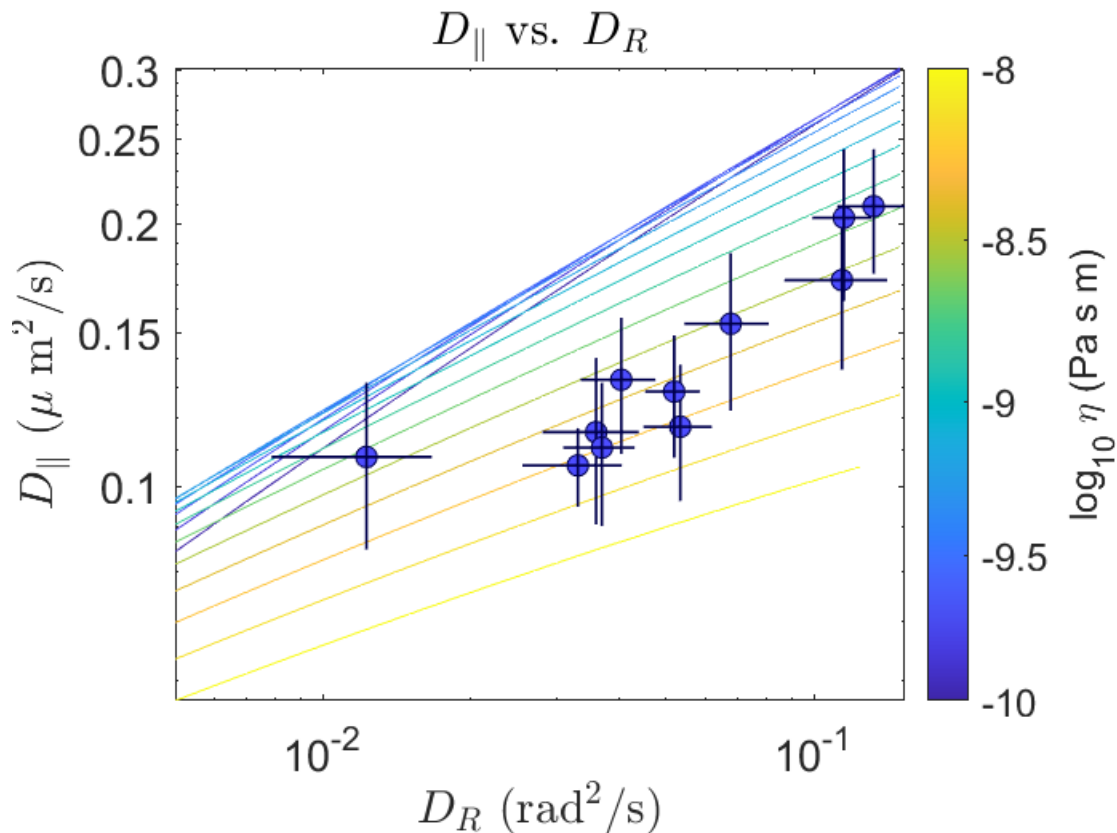


FIGURE 3.6. Parallel diffusion coefficient vs. the rotational diffusion coefficient with curves of constant viscosity based on the LLM model.

3.5. Results

We first assess the viscosity of phase separated vesicles to allow a comparison of the methods. The viscosity was calculated from the diffusion of phase separated domains using their translational diffusion, radius as determined from images,

and the Petrov-Schwille approximation of the HPW model. Each vesicle had multiple domains, ranging from 2 to 18, which were fit to a single viscosity value by calculating translational diffusion coefficients for a wide range of viscosity values and minimizing the mean square distance from the measured translational diffusion coefficients. For $N = 13$ vesicles this resulted in an average \pm standard error of $\eta_{\text{domain}} = 3.0 \pm 0.4 \times 10^{-9}$ Pa \cdot s \cdot m. Uncertainties for individual vesicles were about 30% of the value, but decreased for vesicles with more tracked domains.

Beads were analyzed using both the rotational diffusion coefficient and the parallel diffusion coefficient with the LLM equations used to numerically solve for both the viscosity and the effective length of the beads L . It is possible to use either the parallel diffusion coefficient, the perpendicular diffusion coefficient, or to use their ratio. The difference between the parallel and perpendicular diffusion coefficients, both in our data and the theoretical expectation, is small and so attempting to use the ratio is dominated by noise. We chose to use the parallel diffusion coefficient as it was less noisy than the perpendicular. When beads were added in high concentrations issues arose with beads clumping together and so we used vesicles that had a single bound bead. For $N = 11$ vesicles the average \pm standard error was $\eta_{\text{bead}} = 3.6 \pm 0.4 \times 10^{-9}$ Pa \cdot s \cdot m. The L values had an average \pm standard error of 3.1 ± 0.3 μ m. This average matches the observed length of the beads, but it is important to fit L rather than assuming that it is the observed length of the bead because the effective length can vary greatly from much smaller than the bead, due to a small binding site, to much larger than the bead, due to an induced curvature in the membrane. Forcing the effective length to be equal to the average value results in a higher viscosity value with a larger spread: $4.6 \pm 0.7 \times 10^{-9}$ Pa \cdot s \cdot m. Furthermore, two of the vesicles used were

bound to “double” beads – beads that became stuck together end to end, forming one long bead. One had a calculated length of $L = 3.2 \mu\text{m}$, much smaller than the measured length of $5.3 \mu\text{m}$, but the other had a calculated length of $L = 6.4 \mu\text{m}$, slightly larger than the measured length of $4.6 \mu\text{m}$, and well outside the range of the “single” beads. In Figure 3.7 the histogram of L values excludes this double bead to provide more detail of the other values.

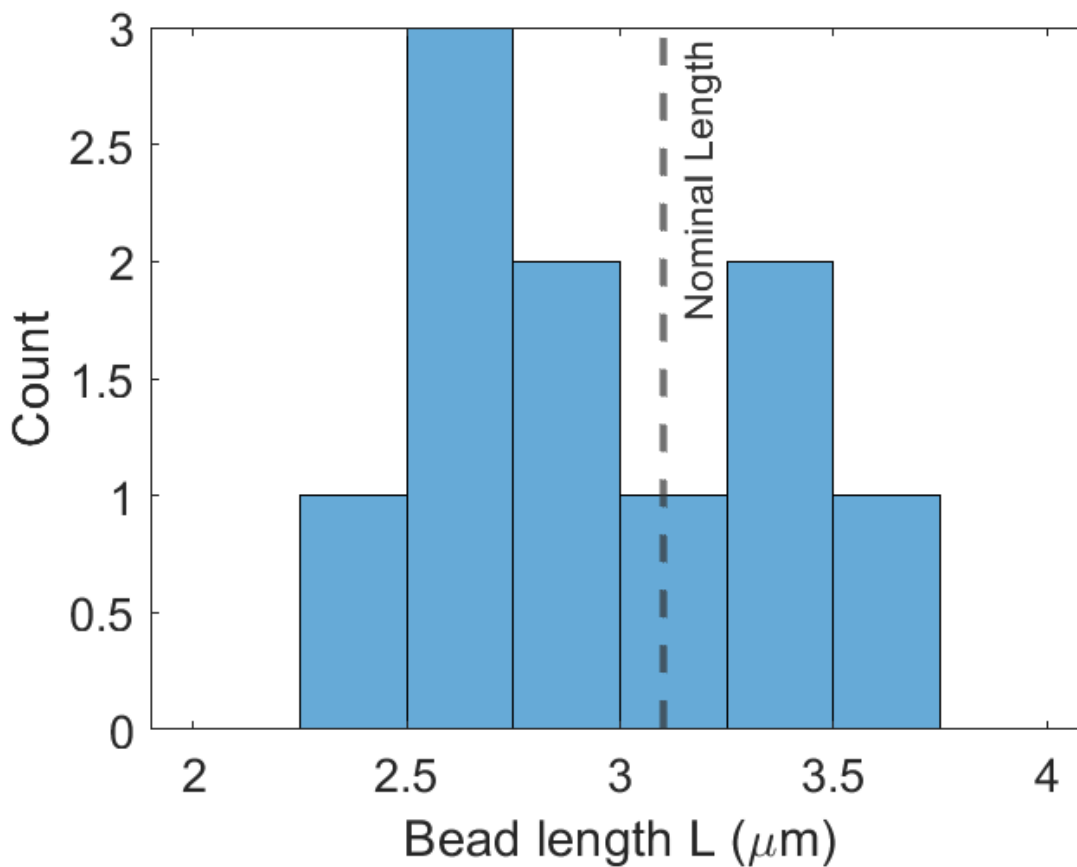


FIGURE 3.7. A histogram of the effective bead lengths L with the nominal length shown with a dotted vertical line. There is one bead with $L = 6.4 \mu\text{m}$ which is not shown in order to provide more detail.

The close agreement of these viscosities, within their uncertainties, as well as both of their agreement with previously measured values for this phase

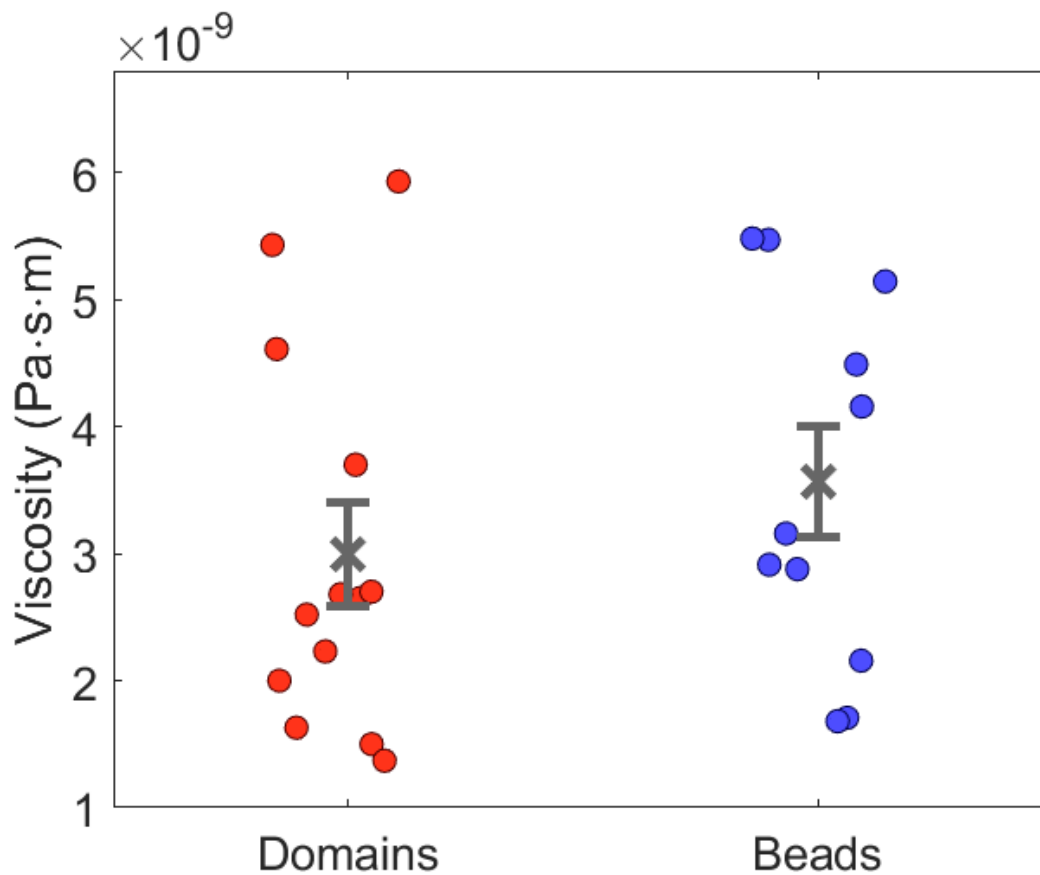


FIGURE 3.8. All viscosity values for the domains and beads with the mean \pm standard error plotted.

($\eta = 3.9 \pm 0.4 \times 10^{-9} \text{ Pa} \cdot \text{s} \cdot \text{m}$ from [31] and similar in [9, 41, 44]), suggests that viscosity determination using elliptical beads provides accurate measures of membrane viscosity, allowing us to apply the method to other systems.

3.6. Chain Length

The simplest lipid membrane is one composed of a single type of lipid. The dependence of its viscosity on the chain length of the lipids is of course impossible to study using phase separated domains as it would require phase separation into

different compositions to occur. Using elliptical beads to measure the viscosity, this becomes a feasible experiment.

Previously, the effect of lipid chain length on membrane diffusion has been studied. In general, as chain length increases there is a slight decrease in diffusion coefficient [73, 74, 75] as shown in Figure 3.9 taken from [1], but this does not necessarily imply an increase in viscosity.

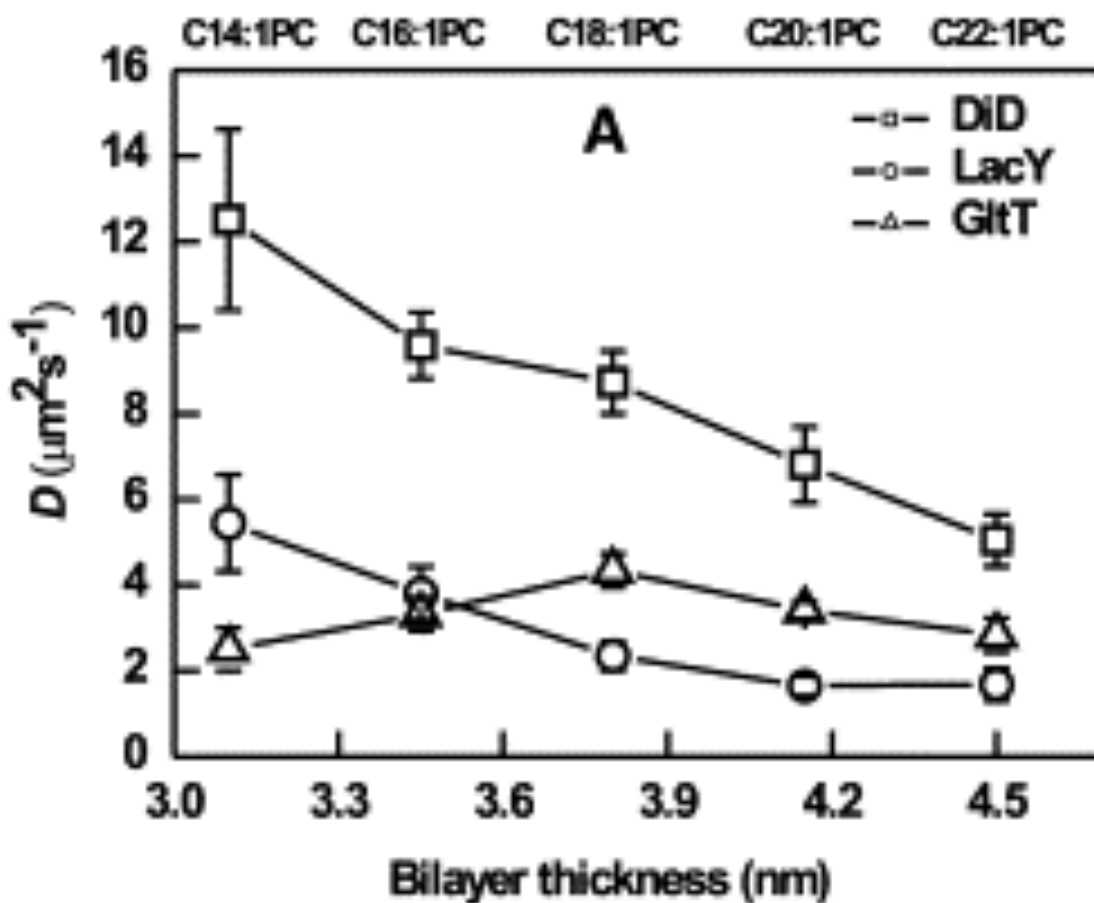


FIGURE 3.9. A plot taken from [1] showing diffusion coefficients of lipid analogue DiD and proteins LacY and GltT

We examined monounsaturated PC lipids with chain lengths of 14, 16, 18, and 20 carbons. These were 1,2-dimyristoleoyl-sn-glycero-3-phosphocholine,

1,2-dipalmitoleoyl-sn-glycero-3-phosphocholine, 1,2-dioleoyl-sn-glycero-3-phosphocholine, and 1,2-dieicosenoyl-sn-glycero-3-phosphocholine respectively, but we will refer to them for simplicity solely by their chain lengths. The double bonds of 14, 16, and 18 all occur at the $\Delta 9$ position whereas the double bond of 20 occurs at the $\Delta 11$ position. We expect this difference to have no significant effect on the behavior.

Vesicle composition was 91% PC lipid, 8% DOTAP, 0.5% 16:0 Biotinyl PE, and 0.5% Texas Red DHPE. They were formed and analyzed in the same manner as the phase separated vesicles. The bead lengths across chain lengths had an average \pm standard error of $3.7 \pm 0.2 \mu\text{m}$, slightly larger than the nominal value of $3.1 \mu\text{m}$. The L values also had a larger spread than the phase separated data, ranging from $2 \mu\text{m}$ to $6.5 \mu\text{m}$, as shown in the histogram in Figure 3.10. The mean \pm standard error for each chain length is

$$\eta_{14} = 2.3 \pm 0.6 \times 10^{-9} \text{ Pa} \cdot \text{s} \cdot \text{m}$$

$$\eta_{16} = 2.5 \pm 0.4 \times 10^{-9} \text{ Pa} \cdot \text{s} \cdot \text{m}$$

$$\eta_{18} = 3.6 \pm 0.8 \times 10^{-9} \text{ Pa} \cdot \text{s} \cdot \text{m}$$

$$\eta_{20} = 3.2 \pm 0.9 \times 10^{-9} \text{ Pa} \cdot \text{s} \cdot \text{m}$$

If we fit a line to these values, as shown in Figure 3.11, it has a slope of $1.9 \pm 1.8 \times 10^{-10}$, implying that while very weak, increasing chain length does have a positive effect on viscosity. Interestingly, if we compare this to the lipid diffusion values taken from [1], finding the viscosity using the Saffmann-Delbrück model, we find that the trend is very similar, shown in Figure 3.12. This similarity is surprising because the microscale viscosity experienced by the lipids themselves is quite

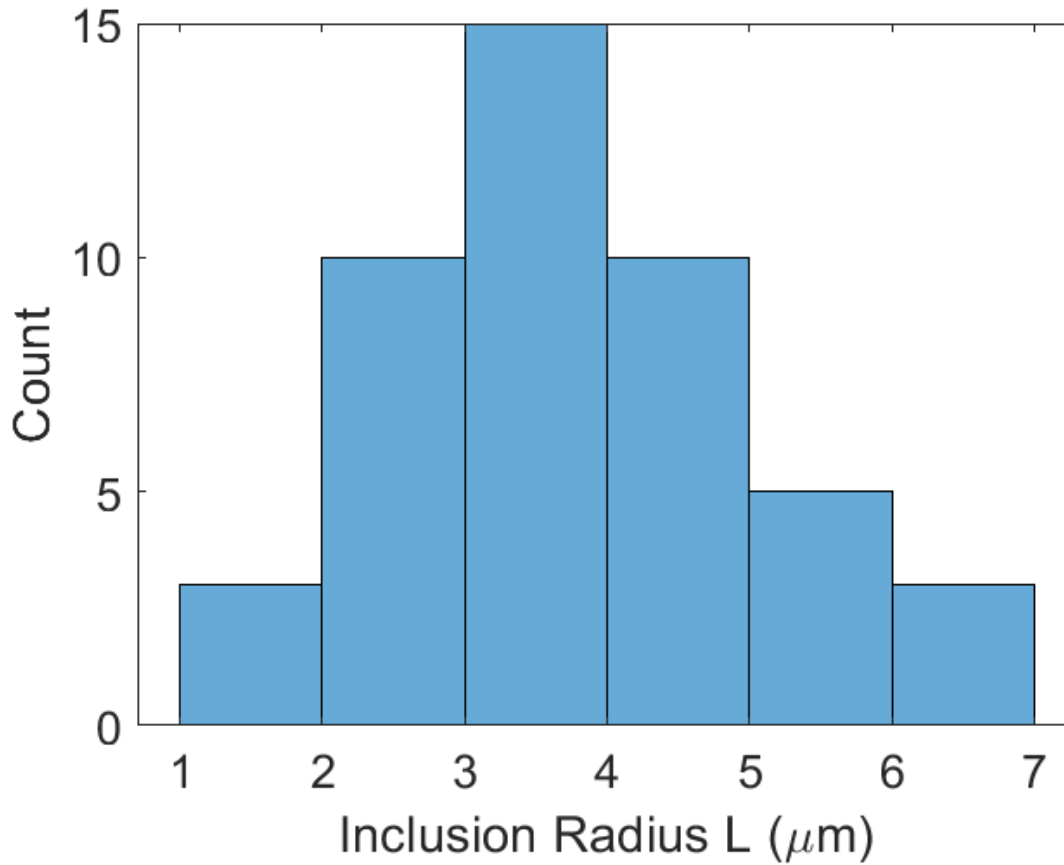


FIGURE 3.10. A histogram of the effective bead lengths from all chain lengths combined.

different from the macroscale viscosity of larger objects in the membrane. The values we find are an order of magnitude smaller - ranging from $1.2 \times 10^{-10} \text{ Pa}\cdot\text{s}\cdot\text{m}$ to $2.5 \times 10^{-10} \text{ Pa}\cdot\text{s}\cdot\text{m}$. So despite the large difference in values, increasing the chain length of lipids appears to have a similar effect on both macroscale and microscale viscosity.

3.7. Conclusion

This work allows us to assert that elliptical beads can provide an accurate measure of the viscosity of a lipid membrane. This opens the door to measuring

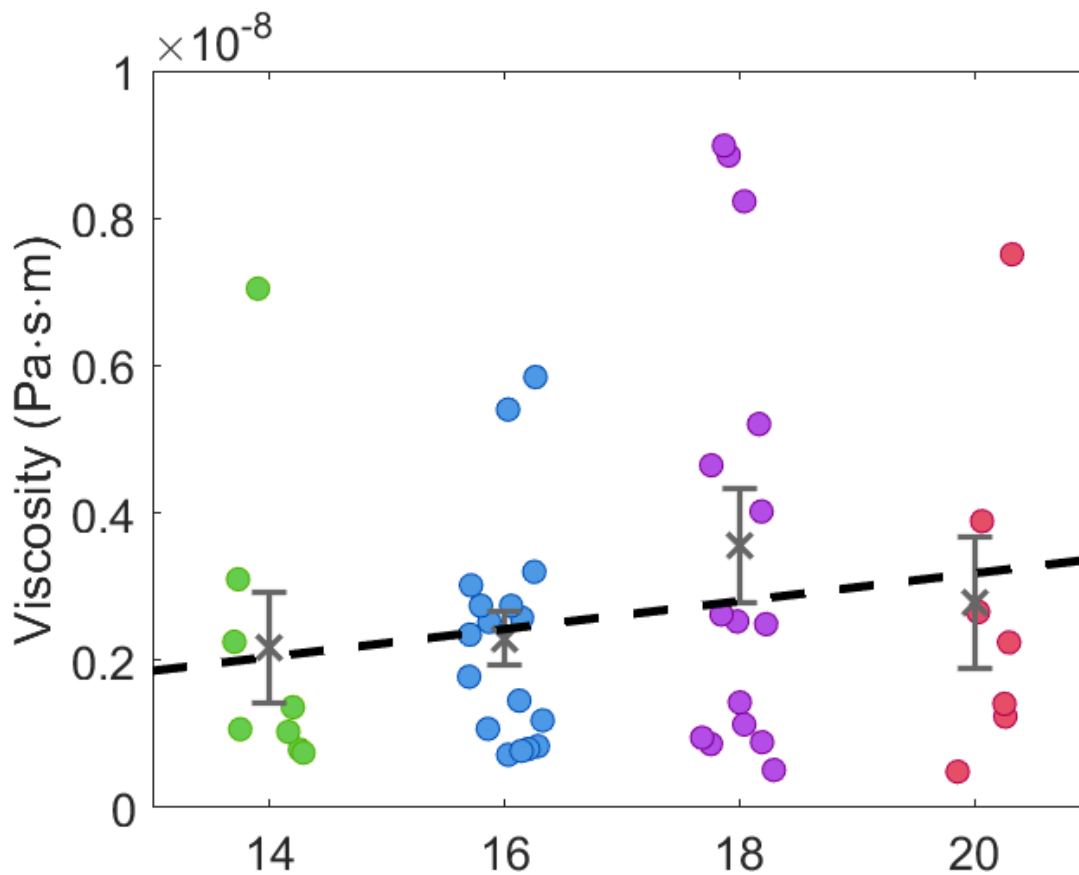


FIGURE 3.11. All viscosity values for the each chain length with the mean \pm standard error plotted. Fitting a line to the data has the slope $1.9 \pm 1.8 \times 10^{-10}$ implying a very weak, but positive affect on viscosity.

viscosity of a wide range of systems that previously would have been unreachable. To demonstrate this, we considered the effect of lipid chain length, which we found to be weakly positive. The importance of lipid viscosity and the scarcity of direct measurements make this a rich area of study. Without the reliance on phase separation, viscosity measurements are possible with any bilayer forming lipids at nearly pure concentrations and any combination of lipids. It is also a conceptually simple extension to study the effect of various proteins on lipid viscosity.

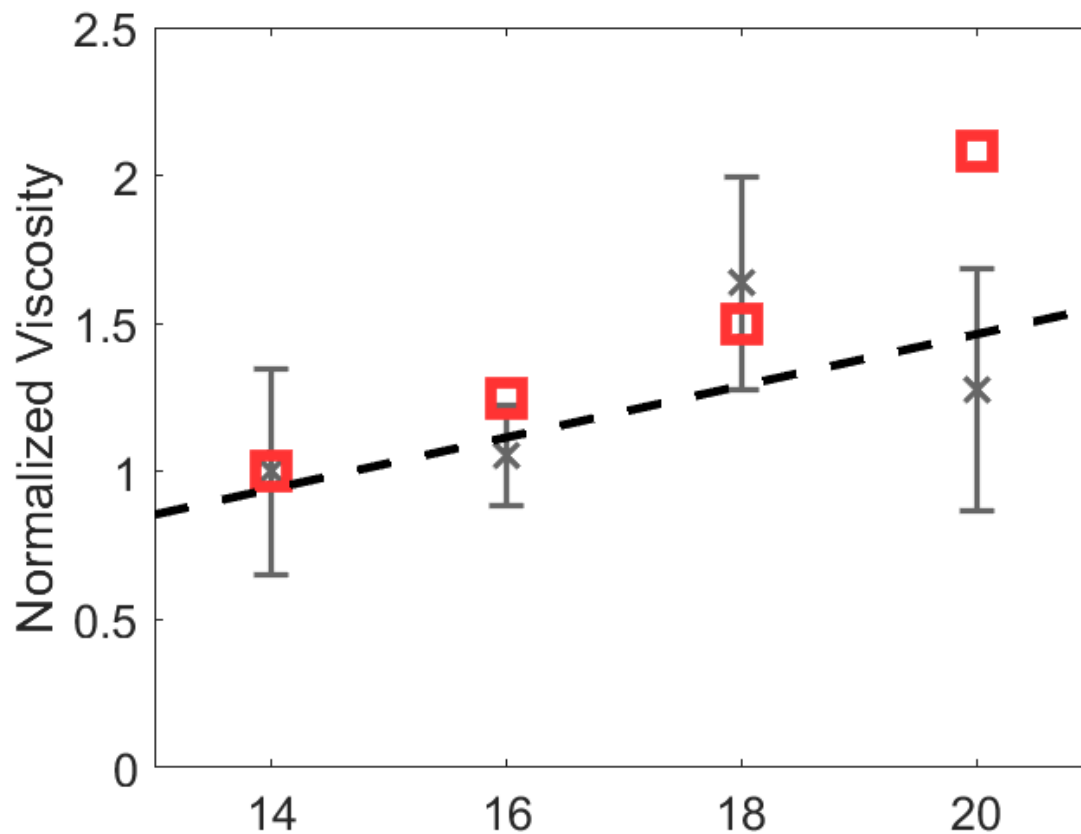


FIGURE 3.12. Comparison of the viscosity at each chain length as measured with elliptical beads (grey x's) and viscosity calculated using lipid diffusion values from [1] and the Saffmann-Delbrück model (red squares). All viscosities are normalized to the 14 chain length value. Despite an order of magnitude difference in viscosity the trend is very similar.

CHAPTER IV

MEMBRANE INTERACTIONS OF THE β CELL EXPANSION FACTOR A PROTEIN

This chapter contains unpublished co-authored material with contributions from Raghuveer Parthasarathy, Emily Sweeney, Karen Guillemin, Jennifer Hill, Michelle Sconce Massaquoi, Elena Wall, Karen Kallio, Daniel Derrick, Rickesha Bell, L. Charles Murtaugh, S. James Remington, and June Round. In this work, I contributed to designing the research, performing the research, analyzing the data, and writing the paper.

4.1. Microbiota and Model Organisms

In this chapter, I will discuss work done with the Guillemin lab involving a bacterial protein they discovered that affects membranes. While I will focus on the work I have performed, understanding the motivation and importance of the work requires further biological background about the microbiota and the way it is studied.

Since their discovery, microbes have largely been portrayed as villains – bringers of disease and death. But this ignores the millions of bacteria that call us home, living on and in our bodies. And this is not just a peaceful coexistence, as our understanding of the human microbiota has increased it has become clear that it plays a crucial role in our health [76, 77].

This has led to greatly increasing interest in microbiota, but it is difficult to study. Much of the work on the gut microbiome has been done using fecal samples [78, 79] which provide a snapshot of the relative abundance of bacteria present

at a particular time. This cannot provide insight into the temporal dynamics or spatial structure of the bacteria. And while understanding how the entire bacterial community affects overall health is important, the vastly complicated system makes it difficult to learn about specific interactions and behaviors.

Much as I have used model membranes to study aspects of complicated biological systems, model organisms can be used to study the microbiota. A successful model organism will be easy to breed and maintain while retaining a genetic similarity to humans. Each commonly used model organism has trade offs: *C. elegans* and *Drosophila melanogaster* reproduce quickly, are very well understood genetically, and have been used in microbiota studies [80, 81, 82, 83, 84]. However, both are far simpler than humans. On the other side of the spectrum, mice are much more similar to humans, but are expensive to house and slow to reproduce and still depend mainly on fecal samples or dissection [85].

Zebrafish occupy a middle ground. They are vertebrates with genetic similarities to humans [86] while still reproducing quickly and in large numbers [87]. They can also be raised germ-free, totally devoid of any bacteria [88], and are largely transparent while in their larval stage, making it possible to take detailed images of them and their microbiota. This makes them a uniquely powerful model organism for this type of work and has led to many interesting discoveries [89].

4.2. β Cells and Bacteria

β cells are insulin producing cells found in the pancreas. Zebrafish hatch with a small number of β cells and in the days following they undergo an expansion [90]. This is very similar to the development of β cells in humans, although the

expansion lasts until age 5 [91]. In both zebrafish and humans this expansion occurs concurrently with the colonization of the gut with bacteria and it has been shown that type 1 diabetes, in which a loss of β cell function results in abnormal glucose homeostasis, is associated with, and in fact preceded by, decreased microbiota diversity [92, 93, 94].

In their 2016 paper, Jennifer Hill et al. [95] compared the number of β cells in germ free (GF) fish with conventional (CV) fish, fish that are exposed to a wide array of bacteria. The number of β cells in CV fish increased steadily over time, but GF fish did not undergo β cell expansion and had elevated levels of circulating glucose, implying that they were unable to correctly regulate glucose levels. They then examined fish that were inoculated with a single species of bacteria and found that, depending on the type of bacteria used, the β cells would develop as in the CV fish or remain stagnant as in the GF fish. Having pinpointed which bacteria were driving the β cell expansion, they were able to isolate exactly what was behind this: a protein that they called β cell expansion factor A, or BefA. Purified BefA on its own will cause β cell expansion and mutant bacteria do not produce BefA but are otherwise identical will not cause β cell expansion, meaning that BefA is both necessary and sufficient for proper β cell development. Interestingly, they were also able to find homologous proteins in bacterial species found in human microbiota that will also cause β cell expansion in zebrafish.

4.3. BefA and Membrane Morphology

Once the protein was identified, it was important to understand how it was interacting with the zebrafish to cause these changes. Sequencing the protein revealed that it contained a SYLF domain. These domains are not well

understood, but have been shown to be associated with membranes [96, 97, 98, 99, 100]. This, as well as the observation of invagination in cells exposed to BefA, inspired an examination of BefA’s interaction with lipid membranes.

Simple vesicles of 99.5% 1,2-dioleoyl-sn-glycero-3-phosphocholine (DOPC) and 0.5% Texas Red 1,2 dihexadecanoyl-sn-glycero-3-phosphoethanolamin (Texas Red DHPE), a fluorescently tagged lipid, were observed in the absence and presence of 0.2 μ M BefA. While it is not uncommon to have imperfect vesicles, those treated with BefA were frequently observed to form clusters of small vesicles adhered to the outside, which we refer to as multi-vesicular vesicles, as shown in Figure 4.1. In order to quantify this, we used a light sheet microscope, described in Chapter 2, to take large 3D scans of vesicles suspended in a cuvette. We then detected bright objects and categorized them based on their morphology. We found that only 3% of the control were multi-vesicular vesicles, while 30% of the BefA treated vesicles were. Each point in Figure 4.2(a) represents the concentration of multi-vesicular vesicles for a single scan. Figure 4.2(b) shows the total number of features, both vesicles and multi-vesicular vesicles, in the control and BefA treated experiments. The doubling in number of features/nanoliter suggests that multi-vesicular vesicles are not formed by separate vesicles binding to each other, but by budding and fragmentation of larger vesicles.

4.4. Continuing Work

In our search of BefA treated vesicles, we also noticed that some of the vesicles were undergoing thermally driven fluctuations, as shown in Figure 4.3. While fluctuations can occur in untreated vesicles, they appeared far more frequently after exposure to BefA. This behavior offers a potential insight into

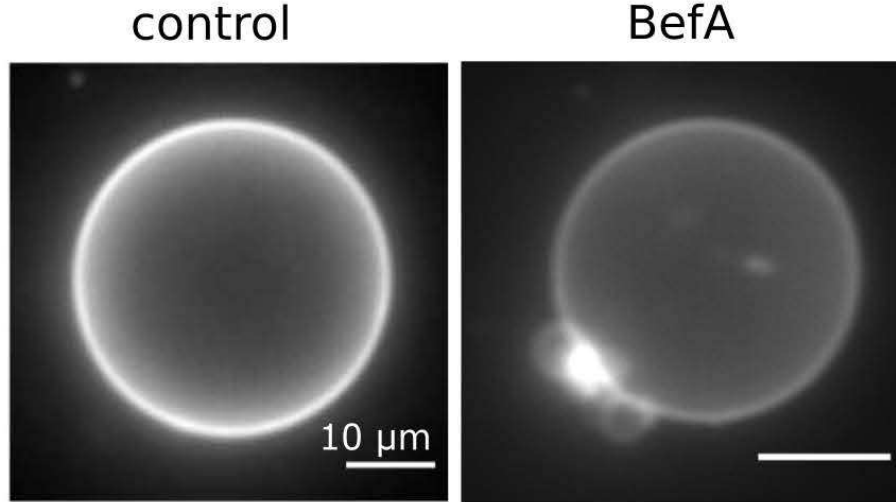


FIGURE 4.1. An example control vesicle and multi-vesicular vesicle. Both scale bars are 10 μm . This figure is taken from an unpublished co-authored work.

how BefA is causing the membrane budding. Fluctuations have been used to measure the bending modulus of membranes [54]. By measuring these fluctuations for untreated vesicles and at several concentrations of BefA we could understand the effect of BefA on the rigidity. We have begun this work, but it will largely be completed in the future.

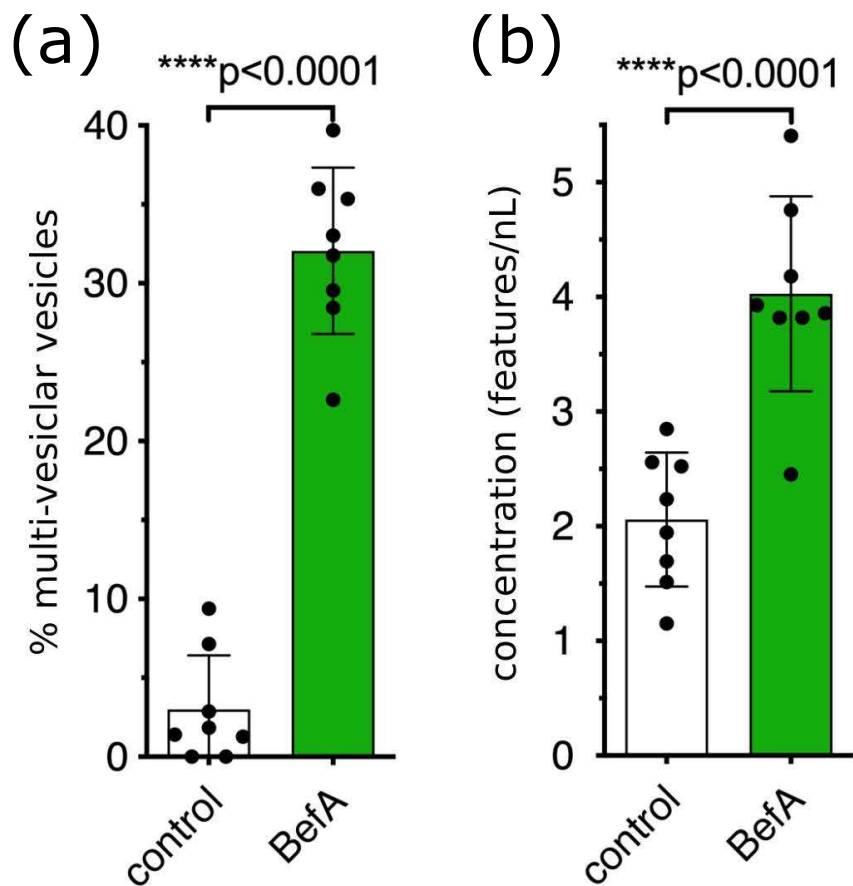


FIGURE 4.2. (a) The percentage of observed features that were multi-vesicular in the control and 2 μM BefaA. Each point is a single scan. The bars represent the total percentage across all scans, 3% in the control and 30% in BefaA treated. (b) The concentration of features in each scan, showing an increase with BefaA exposure. This figure is taken from an unpublished co-authored work.

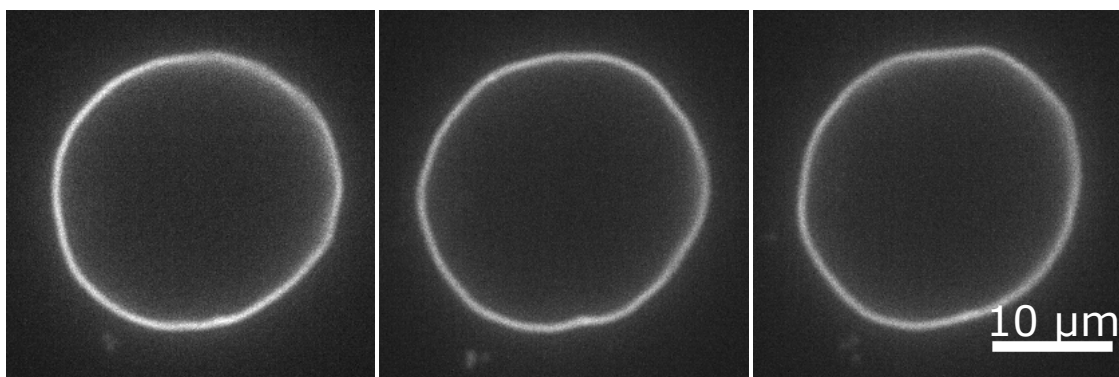


FIGURE 4.3. A single fluctuating vesicle, exposed to 2 μM BefaA. Each image is 2 seconds apart.

CHAPTER V

CONCLUSIONS AND FUTURE DIRECTIONS

The work presented in the previous three chapters represent the completed work of several years. While seeking answers to three different questions, each increase our understanding of the properties and behavior of lipid bilayers and inspire further exploration.

In particular, the ability to determine membrane viscosity from elliptical tracer particles opens the door to many systems. With the newfound capability to measure viscosity of nearly single species membranes, it would be beneficial to do this for the most commonly used lipids. The fact that this work remains to be done emphasizes the difficulty in measuring membrane viscosity. As the viscosities of more lipid species are determined, dependencies on various biophysical properties will emerge, as we observed for chain length. It would be illuminating to study the viscosity dependence on headgroup, acyl chain saturation, and temperature.

Beyond these fundamentals, the effect of various membrane-interacting proteins on viscosity could be studied. For example, this method could be applied to the BefA protein discussed in chapter 4. While the morphological changes caused by BefA could make this experimentally challenging, it is a conceptually simple extension from the previous work.

Between the viscosity and the already begun measurements of bending modulus dependence on BefA, there is much to be done to understand how the protein interacts with lipids. But the work done to characterize the morphology of large scans of vesicles could also have a very different application. Sorting through

detected objects to classify into vesicles and multi-vesicular vesicles resulted in a large collection of cropped videos of objects typical of a bulk solution of vesicles, each with a label. This type of data set is the start of the most important part of any neural network: the training data.

Any neural network is only as good as the information it is given, and creating and curating the labeled data to train the network can be a very time consuming step. With this prepared labeled data it would be possible to train a classifier that could sort potential vesicles without any human input, turning an extremely tedious analysis into something fully automated.

With more effort, this network could even be applied during data collection. While being able to count and sort large number of vesicles would be occasionally useful, it is more common to be interested in videos of a single vesicle. The ability to identify a vesicle paired with the speed of neural networks could make automated data collection possible. A scanning “search” state could feed images to the neural network until an object is identified as a vesicle. The location of the vesicle would be delivered to the stage control and a video would be taken. If the network were already functioning, this extension would be only focused on getting the hardware and software to communicate.

The work described in this dissertation has covered a range of topics and can be continued in many directions. The theme uniting everything is an effort to understand fundamental biophysics of lipid bilayers. This encompasses their boundary conditions with surrounding fluids, methods for measuring their viscosity, and their interaction with proteins. There is ample room for this work to continue and I am excited to watch it develop.

REFERENCES CITED

- [1] Sivaramakrishnan Ramadurai, Ria Duurkens, Victor V. Krasnikov, and Bert Poolman. Lateral diffusion of membrane proteins: Consequences of hydrophobic mismatch and lipid composition. *Biophysical Journal*, 99(5): 1482–1489, 2010. ISSN 0006-3495. doi: <https://doi.org/10.1016/j.bpj.2010.06.036>.
- [2] Phillips, Rob and Kondev, Jane and Theriot, Julie. *Physical Biology of the Cell*. Garland Science, New York, 2009.
- [3] Philip Yeagle. *The Structure of Biological Membranes*. CRC Press, Boca Raton, 2005.
- [4] Winchil L. C. Vaz, Robert M. Clegg, and Dieter Hallmann. Translational diffusion of lipids in liquid crystalline phase phosphatidylcholine multibilayers. a comparison of experiment with theory. *Biochemistry*, 24(3): 781–786, 1985. doi: 10.1021/bi00324a037.
- [5] C. Dietrich, L.A. Bagatolli, Z.N. Volovyk, N.L. Thompson, M. Levi, K. Jacobson, and E. Gratton. Lipid rafts reconstituted in model membranes. *Biophysical Journal*, 80(3):1417–1428, 2001. ISSN 0006-3495. doi: [https://doi.org/10.1016/S0006-3495\(01\)76114-0](https://doi.org/10.1016/S0006-3495(01)76114-0).
- [6] Sarah L. Veatch and Sarah L. Keller. Separation of liquid phases in giant vesicles of ternary mixtures of phospholipids and cholesterol. *Biophysical Journal*, 85(5):3074–3083, 2003. ISSN 0006-3495. doi: [https://doi.org/10.1016/S0006-3495\(03\)74726-2](https://doi.org/10.1016/S0006-3495(03)74726-2).
- [7] Ilya Levental, Kandice R. Levental, and Frederick A. Heberle. Lipid rafts: Controversies resolved, mysteries remain. *Trends in Cell Biology*, 30(5): 341–353, 2020. doi: <https://doi.org/10.1016/j.tcb.2020.01.009>.
- [8] Sean Munro. Lipid rafts: elusive or illusive? *Cell*, 115(4):377–388, 2003. doi: 10.1016/s0092-8674(03)00882-1.
- [9] Pietro Cicuta, Sara L. Keller, and Sarah L. Veatch. Diffusion of liquid domains in lipid bilayer membranes. *J Phys Chem B*, 111(13):3328–33231, 2007. doi: 10.1021/jp0702088.
- [10] Cynthia A. Stanich, Aurelia R. Honerkamp-Smith, Gregory Garbès Putzel, Christopher S. Warth, Andrea K. Lamprecht, Pritam Mandal, Elizabeth Mann, Thien-An D. Hua, and Sarah L. Keller. Coarsening dynamics of domains in lipid membranes. *Biophysical Journal*, 105(2):444–454, 2013. ISSN 0006-3495. doi: <https://doi.org/10.1016/j.bpj.2013.06.013>.

- [11] Oliver Purrucker, Heiko Hillebrandt, Klaus Adlkofer, and Motomu Tanaka. Deposition of highly resistive lipid bilayer on silicon–silicon dioxide electrode and incorporation of gramicidin studied by ac impedance spectroscopy. *Electrochimica Acta*, 47(5):791–798, 2001. ISSN 0013-4686. doi: [https://doi.org/10.1016/S0013-4686\(01\)00759-9](https://doi.org/10.1016/S0013-4686(01)00759-9).
- [12] Jonathan M. Crane, Volker Kiessling, and Lukas K. Tamm. Measuring lipid asymmetry in planar supported bilayers by fluorescence interference contrast microscopy. *Langmuir*, 21(4):1377–1388, 2005. doi: 10.1021/la047654w.
- [13] Magdalena Przybylo, Jan Sykora, Jana Humpolickova, Ales Benda, Anna Zan, and Martin Hof. Lipid diffusion in giant unilamellar vesicles is more than 2 times faster than in supported phospholipid bilayers under identical conditions. *Langmuir*, 22(22):9096–9099, 2006. doi: 10.1021/la061934p.
- [14] Paul Mueller, Donald O. Rudin, H. Ti Tien, and William C. Wescott. Reconstitution of cell membrane structure in vitro and its transformation into an excitable system. *Nature*, 194:979–980, 1962. doi: 10.1038/194979a0.
- [15] Stephen H. White. Analysis of the torus surrounding planar lipid bilayer membranes. *Biophys J.*, 12(4):432–445, 1972. doi: 10.1016/S0006-3495(72)86095-8.
- [16] E. Bamberg, P. Hegemann, and D. Oesterhelt. Reconstitution of the light-driven electrogenic ion pump halorhodopsin in black lipid membranes. *Biochimica et Biophysica Acta (BBA) - Biomembranes*, 773(1):53–60, 1984. ISSN 0005-2736. doi: [https://doi.org/10.1016/0005-2736\(84\)90549-2](https://doi.org/10.1016/0005-2736(84)90549-2).
- [17] Thierry Stora, Jeremy H. Lakey, and Horst Vogel. Ion-channel gating in transmembrane receptor proteins: Functional activity in tethered lipid membranes. *Angewandte Chemie*, 38(3):389–392, 1999. doi: 10.1002/(SICI)1521-3773(19990201)38:3<389::AID-ANIE389>3.0.CO;2-U.
- [18] Patrick Van Gelder, Fabrice Dumas, and Mathias Winterhalter. Understanding the function of bacterial outer membrane channels by reconstitution into black lipid membranes. *Biophysical Chemistry*, 85(2):153–167, 2000. ISSN 0301-4622. doi: [https://doi.org/10.1016/S0301-4622\(99\)00153-2](https://doi.org/10.1016/S0301-4622(99)00153-2).
- [19] S.B. Hladky and D.W. Gruen. Thickness fluctuations in black lipid membranes. *Biophysical Journal*, 38(3):251–258, 1982. ISSN 0006-3495. doi: [https://doi.org/10.1016/S0006-3495\(82\)84556-6](https://doi.org/10.1016/S0006-3495(82)84556-6).
- [20] Jeanne C. Stachowiak, David L. Richmond, Thomas H. Li, Allen P. Liu, Sapun H. Parekh, and Daniel A. Fletcher. Unilamellar vesicle formation and encapsulation by microfluidic jetting. *Proceedings of the National Academy of Sciences*, 105(12):4697–4702, 2008. doi: 10.1073/pnas.0710875105.

- [21] Sandro Matosevic and Brian M. Paegel. Stepwise synthesis of giant unilamellar vesicles on a microfluidic assembly line. *J. Am. Chem. Soc.*, 133(9): 2798–2800, 2011. doi: <https://doi.org/10.1021/ja109137s>.
- [22] W S Trimble, D M Cowan, and R H Scheller. Vamp-1: a synaptic vesicle-associated integral membrane protein. *Proceedings of the National Academy of Sciences*, 85(12):4538–4542, 1988. ISSN 0027-8424. doi: 10.1073/pnas.85.12.4538.
- [23] John A. Wagner and Regis B. Kelly. Topological organization of proteins in an intracellular secretory organelle: The synaptic vesicle. *Proceedings of the National Academy of Sciences of the United States of America*, 76(8): 4126–4130, 1979. ISSN 00278424.
- [24] Demetrios Papahadjopoulos and N. Miller. Phospholipid model membranes. i. structural characteristics of hydrated liquid crystals. *Biochimica et Biophysica Acta (BBA) - Biomembranes*, 135(4):624–638, 1967. ISSN 0005-2736. doi: [https://doi.org/10.1016/0005-2736\(67\)90094-6](https://doi.org/10.1016/0005-2736(67)90094-6).
- [25] M. J. Hope, M. B. Bally, G. Webb, and P. R. Cullis. Production of large unilamellar vesicles by a rapid extrusion procedure: characteriation of size distribution, trapped volume, and ability to maintain a membrane potential. *Biochim Biophys Acta*, 812(1):55–65, 1985.
- [26] Sarah L. Veatch. Electro-formation and fluorescence microscopy of giant vesicles with coexisting liquid phases. In Thomas J. McIntosh, editor, *Lipid Rafts*, pages 59–72. Humana Press, Totowa, NJ, 2007.
- [27] Aidan Brown, Jurij Kotar, and Pietro Cicuta. Active rheology of phospholipid vesicles. *Physical Review E*, 84:021930, 08 2011. doi: 10.1103/PhysRevE.84.021930.
- [28] Seyed R. Tabaei, Jurriaan J. J. Gillissen, Stephan Block, Fredrik Höök, and Nam Joon Cho. Hydrodynamic propulsion of liposomes electrostatically attracted to a lipid membrane reveals size-dependent conformational changes. *ACS Nano*, 10(9):8812–8820, 2016. doi: 10.1021/acsnano.6b04572.
- [29] Martin Vögele, Jürgen Köfinger, and Gerhard Hummer. Hydrodynamics of diffusion in lipid membrane simulations. *Phys. Rev. Lett.*, 120:268104, Jun 2018. doi: 10.1103/PhysRevLett.120.268104.
- [30] Tristan T. Hormel, Sarah Q. Kurihara, M. Kathleen Brennan, Matthew C. Wozniak, and Raghuvveer Parthasarathy. Measuring lipid membrane viscosity using rotational and translational probe diffusion. *Phys. Rev. Lett.*, 112: 188101, 2014.

- [31] Tristan T. Hormel, Matthew A. Reyer, and Raghuveer Parthasarathy. Two-point microrheology of phase-separated domains in lipid bilayers. *Biophysical Journal*, 109(4):732 – 736, 2015. ISSN 0006-3495. doi: <https://doi.org/10.1016/j.bpj.2015.07.017>.
- [32] Vincent L. Thoms, Tristan T. Hormel, Matthew A. Reyer, and Raghuveer Parthasarathy. Tension independence of lipid diffusion and membrane viscosity. *Langmuir*, 33(43):12510–12515, 2017. doi: [10.1021/acs.langmuir.7b02917](https://doi.org/10.1021/acs.langmuir.7b02917).
- [33] Simon Mendez and Manouk Abkarian. In-plane elasticity controls the full dynamics of red blood cells in shear flow. *Phys. Rev. Fluids*, 3:101101, Oct 2018. doi: [10.1103/PhysRevFluids.3.101101](https://doi.org/10.1103/PhysRevFluids.3.101101).
- [34] Kyung Dall Lee, Shlomo Nir, and Demetrios Papahadjopoulos. Quantitative analysis of liposome-cell interactions in vitro: Rate constants of binding and endocytosis with suspension and adherent j774 cells and human monocytes. *Biochemistry*, 32(3):889–899, 1993. doi: [10.1021/bi00054a021](https://doi.org/10.1021/bi00054a021).
- [35] Chunbai He, Yiping Hu, Lichen Yin, Cui Tang, and Chunhua Yin. Effects of particle size and surface charge on cellular uptake and biodistribution of polymeric nanoparticles. *Biomaterials*, 31(13):3657 – 3666, 2010. ISSN 0142-9612. doi: <https://doi.org/10.1016/j.biomaterials.2010.01.065>.
- [36] J. T. Mason and C. Huang. Hydrodynamic analysis of egg phosphatidylcholine vesicles. *Annals of the New York Academy of Sciences*, 308(1):29–48, 1978. doi: [10.1111/j.1749-6632.1978.tb22012.x](https://doi.org/10.1111/j.1749-6632.1978.tb22012.x).
- [37] J. J. Foo, K. K. Liu, and V. Chan. Viscous drag of deformed vesicles in optical trap: Experiments and simulations. *AIChE Journal*, 50(1):249–254, 2004. doi: [10.1002/aic.10023](https://doi.org/10.1002/aic.10023).
- [38] S.M. Johnson, A.D. Bangham, M.W. Hill, and E.D. Korn. Single bilayer liposomes. *Biochimica et Biophysica Acta (BBA) - Biomembranes*, 233(3): 820 – 826, 1971. ISSN 0005-2736. doi: [https://doi.org/10.1016/0005-2736\(71\)90184-2](https://doi.org/10.1016/0005-2736(71)90184-2).
- [39] Martin Kraus, Wolfgang Wintz, Udo Seifert, and Reinhard Lipowsky. Fluid vesicles in shear flow. *Phys. Rev. Lett.*, 77:3685–3688, Oct 1996. doi: [10.1103/PhysRevLett.77.3685](https://doi.org/10.1103/PhysRevLett.77.3685).
- [40] R.E. Waugh. Surface viscosity measurements from large bilayer vesicle tether formation. i. analysis. *Biophysical Journal*, 38(1):19–27, 1982. ISSN 0006-3495. doi: [https://doi.org/10.1016/S0006-3495\(82\)84526-8](https://doi.org/10.1016/S0006-3495(82)84526-8).

- [41] Aurelia R. Honerkamp-Smith, Francis G. Woodhouse, Vasily Kantsler, and Raymond E. Goldstein. Membrane viscosity determined from shear-driven flow in giant vesicles. *Phys. Rev. Lett.*, 111:038103, Jul 2013. doi: 10.1103/PhysRevLett.111.038103.
- [42] Francis G. Woodhouse and Raymond E. Goldstein. Shear-driven circulation patterns in lipid membrane vesicles. *Journal of Fluid Mechanics*, 705: 165–175, 2012. doi: 10.1017/jfm.2012.118.
- [43] Sebastian Reuther and Axel Voigt. Incompressible two-phase flows with an inextensible newtonian fluid interface. *Journal of Computational Physics*, 322:850 – 858, 2016. ISSN 0021-9991.
- [44] Eugene P. Petrov, Rafayel Petrosyan, and Petra Schwille. Translational and rotational diffusion of micrometer-sized solid domains in lipid membranes. *Soft Matter*, 8:7552–7555, 2012. doi: 10.1039/C2SM25796C.
- [45] Thomas H. Li, Jeanne C. Stachowiak, and Daniel A. Fletcher. Mixing solutions in inkjet formed vesicles. In *Methods in Enzymology*, volume 465 of *Methods in Enzymology*, pages 75 – 94. Academic Press, 2009.
- [46] S.A. Shkulipa, W.K. den Otter, and W.J. Briels. Surface viscosity, diffusion, and intermonolayer friction: Simulating sheared amphiphilic bilayers. *Biophysical Journal*, 89(2):823–829, 2005. ISSN 0006-3495.
- [47] B. Cross, A. Steinberger, C. Cottin-Bizonne, J.P. Rieu, and E. Charlaix. Boundary flow of water on supported phospholipid films. *EPL (Europhysics Letters)*, 73(3):390, 2006.
- [48] Yoshihisa Kaizuka and Jay T. Groves. Structure and dynamics of supported intermembrane junctions. *Biophysical Journal*, 86(2):905–912, 2004. ISSN 0006-3495. doi: [https://doi.org/10.1016/S0006-3495\(04\)74166-1](https://doi.org/10.1016/S0006-3495(04)74166-1).
- [49] Benjamin L. Stottrup, Daniel S. Stevens, and Sarah L. Keller. Miscibility of ternary mixtures of phospholipids and cholesterol in monolayers, and application to bilayer systems. *Biophysical Journal*, 88(1):269–276, 2005. ISSN 0006-3495. doi: <https://doi.org/10.1529/biophysj.104.048439>.
- [50] William Murray Deen. *Analysis of Transport Phenomena*. Oxford University Press, 1998.
- [51] J.S. Hadamard. Mouvement permanent lent d’une sphere liquide et visqueuse dans un liquide visqueux. *C.R. Acad. Sci.*, 152:1735 – 1738, 1911.
- [52] W. Rybczynski. Über die fortschreitende bewegung einer flüssigen kugel in einem zähen medium. *Bull. Acad. Sci. Cracovie*, A:40 – 46, 1911.

- [53] Vasilis Ntziachristos. Going deeper than microscopy: the optical imaging frontier in biology. *Nature Methods*, 7(603):603–614, 2010. doi: 10.1038/nmeth.1483.
- [54] Andrew F. Loftus, Sigrid Noreng, Vivian L. Hsieh, and Raghuvver Parthasarathy. Robust measurement of membrane bending moduli using light sheet fluorescence imaging of vesicle fluctuations. *Langmuir*, 29(47): 14588–14594, 2013.
- [55] Michael J. Taormina, Matthew Jemielita, W. Zac Stephens, Adam R. Burns, Joshua V. Troll, Raghuvver Parthasarathy, and Karen Guillemin. Investigating bacterial-animal symbioses with light sheet microscopy. *The Biological Bulletin*, 223(1):7–20, 2012. doi: 10.1086/BBLv223n1p7.
- [56] Philipp J. Keller, Annette D. Schmidt, Joachim Wittbrodt, and Ernst H.K. Stelzer. Reconstruction of zebrafish early embryonic development by scanned light sheet microscopy. *Science*, 322(5904):1065–1069, 2008. ISSN 0036-8075. doi: 10.1126/science.1162493.
- [57] Raghuvver Parthasarathy. Rapid, accurate particle tracking by calculation of radial symmetry centers. *Nature Methods*, 9:724–726, 2012.
- [58] Christian L. Vestergaard, Paul C. Blainey, and Henrik Flyvbjerg. Optimal estimation of diffusion coefficients from single-particle trajectories. *Phys. Rev. E*, 89, Feb 2014. doi: 10.1103/PhysRevE.89.022726.
- [59] J. Illingworth and J. Kittler. The adaptive hough transform. *IEEE Transactions on Pattern Analysis and Machine Intelligence*, PAMI-9(5): 690–698, Sept 1987. doi: 10.1109/TPAMI.1987.4767964.
- [60] Kai Di Chen, Yi Feng Lin, and Chein Hsiun Tu. Densities, viscosities, refractive indexes, and surface tensions for mixtures of ethanol, benzyl acetate, and benzyl alcohol. *Journal of Chemical & Engineering Data*, 57(4): 1118–1127, 2012. doi: 10.1021/je201009c.
- [61] Jay T. Groves, Raghuvver Parthasarathy, and Martin B. Forstner. Fluorescence imaging of membrane dynamics. *Annual Review of Biomedical Engineering*, 10(1):311–338, 2008. doi: 10.1146/annurev.bioeng.10.061807.160431.
- [62] J.F. Swindells, Snyder C. F., R. C. Hardy, and P. E. Golden. Viscosities of sucrose solutions at various temperatures: Tables of recalculated values. *National Bureau of Standards Circular*, 440, July 1958.
- [63] Jonas Henriksen, Amy C. Rowat, and John H. Ipsen. Vesicle fluctuation analysis of the effects of sterols on membrane bending rigidity. *European Biophysics Journal*, 33(8):732–741, Dec 2004. doi: 10.1007/s00249-004-0420-5.

- [64] J.B. Manneville, P. Bassereau, D. Lévy, and J. Prost. Activity of transmembrane proteins induces magnification of shape fluctuations of lipid membranes. *Phys. Rev. Lett.*, 82:4356–4359, May 1999. doi: 10.1103/PhysRevLett.82.4356.
- [65] Jans, David A. *The Mobile Receptor Hypothesis*. Springer US, 1997.
- [66] G. Vereb, J. Szöllösi, J. Matkó, P. Nagy, T. Farkas, L. Vígh, L. Mátyus, T. A. Waldmann, and S. Damjanovich. Dynamic, yet structured: The cell membrane three decades after the singer–nicolson model. *Proceedings of the National Academy of Sciences*, 100(14):8053–8058, 2003. ISSN 0027-8424. doi: 10.1073/pnas.1332550100.
- [67] Naomi Oppenheimer and Haim Diamant. In-plane dynamics of membranes with immobile inclusions. *Phys. Rev. Lett.*, 107:258102, Dec 2011. doi: 10.1103/PhysRevLett.107.258102.
- [68] Jay T. Groves and John Kuriyan. Molecular mechanisms in signal transduction at the membrane. *Nature Structural & Molecular Biology*, 17:659–665, 2010. doi: 10.1038/nsmb.1844.
- [69] Julie A. Champion, Yogesh K. Katare, and Samir Mitragotri. Particle shape: A new design parameter for micro- and nanoscale drug delivery carriers. *Journal of Controlled Release*, 121(1):3–9, 2007. ISSN 0168-3659. doi: <https://doi.org/10.1016/j.jconrel.2007.03.022>. Fourth International Nanomedicine and Drug Delivery Symposium.
- [70] P. G. Saffman and M. Delbrück. Brownian motion in biological membranes. *PNAS*, 72(8):3111–3113, 1975. doi: <https://doi.org/10.1073/pnas.72.8.3111>.
- [71] B. D. Hughes, B. A. Pailthorpe, and L. R. White. The translational and rotational drag on a cylinder moving in a membrane. *Journal of Fluid Mechanics*, 110:349–372, 1981. doi: 10.1017/S0022112081000785.
- [72] Alex J. Levine, T. B. Liverpool, and F. C. MacKintosh. Mobility of extended bodies in viscous films and membranes. *Phys. Rev. E*, 69:021503, Feb 2004. doi: 10.1103/PhysRevE.69.021503.
- [73] Winchil L.C. Vaz and Hallmann Dieter. Experimental evidence against the applicability of the saffman-delbrück model to the translational diffusion of lipids in phosphatidylcholine bilayer membranes. *FEBS Letters*, 152(2): 287–290, 1983. ISSN 0014-5793. doi: [https://doi.org/10.1016/0014-5793\(83\)80397-4](https://doi.org/10.1016/0014-5793(83)80397-4).

- [74] W. L. Vaz, R. M. Clegg, and D. Hallman. Translational diffusion of lipids in liquid crystalline phase phosphatidylcholine multibilayers. a comparison of experiment with theory. *Biochemistry*, 25(3):781–786, 1985. doi: 10.1021/bi00324a037.
- [75] H. J. Müller and H. J. Galla. Chain length and pressure dependence of lipid translational diffusion. *European Biophysics Journal*, 14:485–491, 1987. doi: <https://doi.org/10.1007/BF00293258>.
- [76] Human Microbiome Project Consortium. Structure, function and diversity of the healthy human microbiome. *Nature*, 486(7402):207–214, 2012. doi: 10.1038/nature11234.
- [77] Mirjana Rajilić-Stojanović, Hans G. H. J. Heilig, Sebastian Tims, Erwin G. Zoetendal, and Willem M. de Vos. Long-term monitoring of the human intestinal microbiota composition. *Environmental Microbiology*, 15(4): 1146–1159, 2013. doi: <https://doi.org/10.1111/1462-2920.12023>.
- [78] Lloyd-Price J Mallick H Branck T Ivey KL Drew DA DuLong C Rimm E Izard J Chan AT Huttenhower C. Abu-Ali GS, Mehta RS. Metatranscriptome of human faecal microbial communities in a cohort of adult men. *Nat Microbiol*, 3(3):356–366, 2018. doi: 10.1038/s41564-017-0084-4.
- [79] Stavros Bashiardes, Gili Zilberman-Schapira, and Eran Elinav. Use of metatranscriptomics in microbiome research. *Bioinform Biol Insights*, 10: 19–25, 2016. doi: 10.4137/BBI.S34610.
- [80] Walhout AJ. Yilmaz LS. Worms, bacteria, and micronutrients: an elegant model of our diet. *Trends Genet*, 30(11):496–503, 2014. doi: 10.1016/j.tig.2014.07.010.
- [81] Nicole M. Vega and Jeff Gore. Stochastic assembly produces heterogeneous communities in the caenorhabditis elegans intestine. *PLOS Biology*, 15(3): 1–20, 03 2017. doi: 10.1371/journal.pbio.2000633.
- [82] Bost A-Douglas AE. Adair KL, Wilson M. Microbial community assembly in wild populations of the fruit fly drosophila melanogaster. *ISME J*, 12(4): 959–972, 2018. doi: 10.1038/s41396-017-0020-x.
- [83] Adam J. Dobson, John M. Chaston, and Angela E. Douglas. The drosophila transcriptional network is structured by microbiota. *BMC Genomics*, 17 (975), 2016. doi: <https://doi.org/10.1186/s12864-016-3307-9>.
- [84] Jaenike J. Martinson VG, Douglas AE. Community structure of the gut microbiota in sympatric species of wild drosophila. *Ecol Lett*, 20(5), 2017. doi: 10.1111/ele.12761.

- [85] Liston A Raes J. Nguyen TL, Vieira-Silva S. How informative is the mouse for human gut microbiota research? *Dis Model Mech*, 8(1), 2015. doi: 10.1242/dmm.017400.
- [86] Kimberly Dooley and Leonard I Zon. Zebrafish: a model system for the study of human disease. *Current Opinion in Genetics & Development*, 10(3): 252–256, 2000. ISSN 0959-437X. doi: [https://doi.org/10.1016/S0959-437X\(00\)00074-5](https://doi.org/10.1016/S0959-437X(00)00074-5).
- [87] Bradford-Y.M. Conlin T. Eagle A.E. Fashena D. Frazer K. Knight J. Mani P. Martin R. Moxon S.A. Paddock H. Pich C. Ramachandran S. Ruef B.J. Ruzicka L. Schaper K. Shao X. Singer A. Sprunger B. Van Slyke C.E. Howe, D.G. and M. Westerfield. Zfin, the zebrafish model organism database: increased support for mutants and transgenics. *Nucleic acids research*, 41 (D1):854–860, 2013.
- [88] Phennicie RT Stephens WZ Rawls JF Guillemin K Kim CH. Milligan-Myhre K, Charette JR. Study of host-microbe interactions in zebrafish. *Methods Cell Biol.*, 105:87–116, 2011. doi: 10.1016/B978-0-12-381320-6.00004-7.
- [89] Keaton Stagaman, Thomas J. Sharpton, and Karen Guillemin. Zebrafish microbiome studies make waves. *Lab Animal*, 49:201–207, 2020. doi: <https://doi.org/10.1038/s41684-020-0573-6>.
- [90] Won-Suk Chung, Olov Andersson, Richard Row, David Kimelman, and Didier Y. R. Stainier. Suppression of alk8-mediated bmp signaling cell-autonomously induces pancreatic β -cells in zebrafish. *Proceedings of the National Academy of Sciences*, 107(3):1142–1147, 2010. ISSN 0027-8424. doi: 10.1073/pnas.0910205107.
- [91] Brigid E. Gregg, Patrick C. Moore, Damien Demozay, Ben A. Hall, Mei Li, Aliya Husain, Amy J. Wright, Mark A. Atkinson, and Christopher J. Rhodes. Formation of a Human β -Cell Population within Pancreatic Islets Is Set Early in Life. *The Journal of Clinical Endocrinology & Metabolism*, 97(9): 3197–3206, 09 2012. ISSN 0021-972X. doi: 10.1210/jc.2012-1206.
- [92] Christopher T. Brown, Austin G. Davis-Richardson, Adriana Giongo, Kelsey A. Gano, David B. Crabb, Nabanita Mukherjee, George Casella, Jennifer C. Drew, Jorma Ilonen, Mikael Knip, Heikki Hyöty, Riitta Veijola, Tuula Simell, Olli Simell, Josef Neu, Clive H. Wasserfall, Desmond Schatz, Mark A. Atkinson, and Eric W. Triplett. Gut microbiome metagenomics analysis suggests a functional model for the development of autoimmunity for type 1 diabetes. *PLOS ONE*, 6(10):1–9, 10 2011. doi: 10.1371/journal.pone.0025792.

- [93] Adriana Giongo, Kelsey A. Gano, David B Crabb, Nabanita Mukherjee, Luis L Novelo, George Casella, Jennifer C. Drew, Jorma Ilonen, Mikael Knip, Heikki Hyóty, Riitta Veijola, Tuula Simell, Olli Simell, Josef Neu, Clive H. Wasserfall, Desmond Schatz, Mark A. Atkinson, and Eric W. Triplett. Toward defining the autoimmune microbiome for type 1 diabetes. *ISME Journal*, 5:82–91, 2011. doi: <https://doi.org/10.1038/ismej.2010.92>.
- [94] Kostic AD, Gevers D, Siljander H, Vatanen T, Hyotylainen T, Hamalainen AM, Peet A, Tillmann V, Poho P, Mattila I, Lahdesmaki H, Franzosa EA, Vaarala O, de Goffau M, Harmsen H, Ilonen J, Virtanen SM, Clish CB, Oresic M, Huttenhower C, Knip M, and Xavier R. JDIABIMMUNE Study Group. The dynamics of the human infant gut microbiome in development and in progression toward type 1 diabetes. *Cell Host & Microbe*, 17:260–273, 2015. doi: <https://doi.org/10.1016/j.chom.2015.01.001>.
- [95] Jennifer Hampton Hill, Eric A Franzosa, Curtis Huttenhower, and Guillemin Karen. A conserved bacterial protein induces pancreatic beta cell expansion during zebrafish development. *eLife*, 5, 2016. doi: [10.7554/eLife.20145](https://doi.org/10.7554/eLife.20145).
- [96] Junya Hasegawa, Emi Tokuda, Takeshi Tenno, Kazuya Tsujita, Haruko Sawai, Hidekazu Hiroaki, Tadaomi Takenawa, and Toshiki Itoh. SH3YL1 regulates dorsal ruffle formation by a novel phosphoinositide-binding domain. *Journal of Cell Biology*, 193(5):901–916, 05 2011. ISSN 0021-9525. doi: [10.1083/jcb.201012161](https://doi.org/10.1083/jcb.201012161).
- [97] Arpaporn Sutipatanasomboon, Stefanie Herberth, Ellen G. Alwood, Heidrun Haweker, Britta Muller, Mojgan Shahriari, Anke Y. Zienert, Birger Marin, Silke Robatzek, Gerrit J. K. Praefcke, Kathryn R. Ayscough, Martin Hulskamp, and Swen Schellmann. Disruption of the plant-specific CFS1 gene impairs autophagosome turnover and triggers EDS1-dependent cell death. *Scientific Reports*, 7(8677), 2017. doi: <https://doi.org/10.1038/s41598-017-08577-8>.
- [98] Alastair S Robertson, Ellen G Allwood, Adam P C Smith, Fiona C Gardiner, Rosaria Costa, Steve J Winder, and Kathryn R Ayscough. The wasp homologue las17 activates the novel actin-regulatory activity of ysc84 to promote endocytosis in yeast. *Molecular biology of the cell*, 20(6):1618–1628, March 2009. ISSN 1059-1524. doi: [10.1091/mbc.e08-09-0982](https://doi.org/10.1091/mbc.e08-09-0982).

- [99] Raffi Tonikian, Xiaofeng Xin, Christopher P. Toret, David Gfeller, Christiane Landgraf, Simona Panni, Serena Paoluzi, Luisa Castagnoli, Bridget Currell, Somasekar Seshagiri, Haiyuan Yu, Barbara Winsor, Marc Vidal, Mark B. Gerstein, Gary D. Bader, Rudolf Volkmer, Gianni Cesareni, David G. Drubin, Philip M. Kim, Sachdev S. Sidhu, and Charles Boone. Bayesian modeling of the yeast sh3 domain interactome predicts spatiotemporal dynamics of endocytosis proteins. *PLoS Biology*, 7(10):1–20, 10 2009. doi: 10.1371/journal.pbio.1000218. URL <https://doi.org/10.1371/journal.pbio.1000218>.
- [100] Agnieszka N. Urbanek, Rebekah Chan, and Kathryn R. Ayscough. Function and interactions of the Ysc84/SH3yl1 family of actin- and lipid-binding proteins. *Biochemical Society Transactions*, 43(1):111–116, 01 2015. ISSN 0300-5127. doi: 10.1042/BST20140221.